frontiers in Electronics

TYPE Original Research
PUBLISHED 08 April 2026
DOI 10.3389/felec.2026.1788559

OPEN ACCESS

EDITED BY
Jun Ohta,
Nara Institute of Science and Technology (NAIST), Japan

REVIEWED BY
Yasuo Terasawa,
Nidek Co., Ltd., Japan
Akib Abdullah Khan,
Washington State University, United States

*CORRESPONDENCE
Ahmad Shah Idil,
a.shahidil@imperial.ac.uk

RECEIVED 27 January 2026
REVISED 26 February 2026
ACCEPTED 27 February 2026
PUBLISHED 08 April 2026

CITATION
Shah Idil A, Lamont C, Nanbakhsh K, Mazza F, Giagka V, Constandinou TG, Vanhoestenberghe A and Donaldson NdN (2026) On the stability of CMOS ICs with plasma-enhanced silicone encapsulation for active implantable neurotechnology: 4.3 years of accelerated life testing. *Front. Electron.* 7:1788559. doi: 10.3389/felec.2026.1788559

On the stability of CMOS ICs with plasma-enhanced silicone encapsulation for active implantable neurotechnology: 4.3 years of accelerated life testing

Ahmad Shah Idil[1,2,3,4]*, Callum Lamont[1], Kambiz Nanbakhsh[5], Federico Mazza[2], Vasiliki Giagka[5,6], Timothy G. Constandinou[2,3,4], Anne Vanhoestenberghe[7] and Nicholas de Neufville Donaldson[1]

[1]Department of Medical Physics and Bioengineering, University College London, London, United Kingdom, [2]Department of Electrical and Electronic Engineering, Imperial College London, London, United Kingdom, [3]UK Dementia Research Institute, Care Research and Technology Centre, London, United Kingdom, [4]Mint Neurotechnologies Ltd., London, United Kingdom, [5]Department of Microelectronics, Faculty of Electrical Engineering, Mathematics and Computer Science, Delft University of Technology, Delft, Netherlands, [6]Department of System Integration and Interconnection Technologies, Fraunhofer-Institut für Zuverlässigkeit und Mikrointegration, Berlin, Germany, [7]School of Biomedical Engineering and Imaging Sciences, King's College London, London, United Kingdom

The long-term stability of polymer-encapsulated CMOS integrated circuits (ICs) is essential for mm-size active implantable medical devices (AIMDs), where hermetic packaging is impractical. Validating robust, biocompatible, implantable IC encapsulation is a prerequisite for chip-scale polymeric bioelectronic implants. This study presents the first long-term validation of a design strategy combining medical-grade silicone, plasma surface treatment for adhesion, and foundry-manufactured CMOS ICs. These ICs feature a perforated shield layer (top metal layer) and a double-layer wall-of-vias to reduce moisture ingress and mechanical delamination. Test structures with silicon oxide/nitride passivation were encapsulated using implant-compatible processes and immersed in saline under accelerated ageing conditions (47 °C, 67 °C, and 87 °C) for up to 4.3 years, under DC and biphasic biases. Throughout the study, electrochemical impedance spectroscopy (EIS) showed no insulation failures. Minor visual corrosion was confined to wire bonds and solder pads, with no correlation to electrical degradation. These results demonstrate the robustness to biofluid exposure of modern IC passivation when combined with well-adhered silicone encapsulation. To our knowledge, this is the longest and most comprehensive accelerated ageing study of its kind, and the first to establish a scalable, industry-compatible encapsulation method for implanted ICs. Our findings provide critical evidence supporting the integration of CMOS ICs into next-generation bioelectronic implants.

KEYWORDS
CMOS, encapsulation, implanted devices, life test, PDMS, silicone

1 Introduction

The next-generation of neural implants must unite two critical design goals: ultra-miniaturisation and decades-long stability in the harsh environment of the human body. These requirements reflect the growing demand for minimally invasive devices that can be easily implanted with minimal surgical trauma while providing a lifetime of reliable operation.

Applications as varied as vagus nerve stimulation (VNS) (Ben-Menachem et al., 2015; Mathews et al., 2025), deep brain stimulation (DBS) (Coffey, 2009; Parastarfeizabadi and Kouzani, 2017), cochlear implants (Napl et al., 2020; Mc Laughlin et al., 2012) and retinal prostheses (Chuang et al., 2014), brain–computer interfaces (BCIs) (Martini et al., 2020), and emerging closed-loop neuromodulation systems for epilepsy (Kassiri et al., 2017), chronic pain (Abrecht et al., 2017), and movement disorders (Broccard et al., 2014) could all be transformed by the development of smaller, longer-lasting implants driven by advances in CMOS technology, and protected by soft polymeric encapsulation.

Silicone rubber (often referred to as PDMS, or polydimethylsiloxane) (Lamont, 2020; Lamont et al., 2021; Nanbakhsh et al., 2025; Bae et al., 2014; Brindley et al., 1986; Colas and Curtis, 2004; Jeong J. W. et al., 2015; Kim et al., 2011; Kinloch, 2012; Lacour et al., 2010), parylene (Aceros et al., 2012; Agarwal et al., 2018; Chang et al., 2013; Kuo et al., 2010; Lecomte et al., 2017; Noh et al., 2004; Ortigoza-Diaz et al., 2018; Rezai et al., 2011; Rodger et al., 2006; Shapero et al., 2016; Stark, 1996; Tan and Craighead, 2010), polyimide (Ahn et al., 2019; HajjHassan et al., 2008; Klinge et al., 2001; Rubehn and Stieglitz, 2010; Vanherck et al., 2013; Chong et al., 2020), and liquid crystal polymer (LCP) (Ahn et al., 2019; Bouteiller and Lebarny, 1996; Chen et al., 2006; Ha et al., 2010; Jeong J. et al., 2015; Jeong et al., 2012; Jeong et al., 2013; Lee et al., 2009; Lee et al., 2011; Liu and Broer, 2014; Park et al., 2016) have emerged as potential candidates for this purpose. However, each of these materials requires encapsulation strategies validated by demonstrating that they can reliably protect integrated circuits (ICs) from moisture and electrochemical degradation over decades. Furthermore, the encapsulation method must be scalable and compatible with established AIMD industry practices, and the validation should be performed using medical grade materials approved for use in human implantable devices, to minimise the barriers to translation of the research results into real devices. Few studies have achieved this. Most were limited by: (1) a low number of samples; (2) having only one test temperature, thus unable to assess the linearity of the acceleration factor; and (3) no DC bias, necessary for validating the encapsulation method for power supply lines in future devices. Those that show promising performance do not demonstrate how to achieve this in a scalable, biocompatible manner using foundry-fabricated ICs and industry-compatible processes.

In this work, we present the first long-term validation of a complete design strategy for CMOS ICs embedded in medical grade silicone rubber, enhanced by plasma surface treatment and chip-level design features, including a top metal shield layer and double layer wall-of-vias, to ensure adhesion, and thus electrical reliability of our test devices. These results establish a technical foundation for future generations of soft, chip-scale implants in which active ICs are seamlessly integrated and protected by plasma-enhanced silicone encapsulation.

2 Background

In almost all active implantable medical devices (AIMD), electronics are housed inside a gas-filled, hermetically-sealed titanium enclosure, following a method initially proposed by Cowdrey at Telectronics in 1971 (Shepherd, 2016). Early attempts at polymer (usually epoxy) encapsulation to protect all the component surfaces exhibited relatively poor reliability and were generally discarded (Greatbatch, 2000). Hermetic packaging maintains electronics, particularly regions of high field strengths, in a dry environment, thus achieving long implant lifetimes (Vanhoestenberghe and Donaldson, 2013). However, this approach becomes increasingly impractical as device size decreases. For small implants with electronics placed close to electrodes, as envisioned for bioelectronic medicines, for example, metal enclosures are excessively bulky. Another approach is micropackaging, similar to methods used in microelectromechanical systems (MEMS), where a lid is bonded to the integrated circuit chip (Saeidi et al., 2010). However, wafer-on-wafer bonding processes for these micropackages can be prohibitively expensive, particularly for university research, and as internal volumes shrink, the methods for validating hermeticity become inadequate (Vanhoestenberghe and Donaldson, 2011).

An alternative is polymer encapsulation, which may suffice for protection (see Supplementary Material 1 for a background review of the state of the knowledge of encapsulants). The Brindley sacral anterior root stimulator implant (SARS), commercialised by Finetech Medical, has demonstrated a well-established track record of long-term reliability with components encapsulated in silicone rubber. Although the exact lifetime of currently implanted devices is unknown, a review of the first 500 implants by Brindley reported mean times to failure of 19 years (Brindley, 1995). The mechanism by which silicone encapsulants protect implanted electronics is often misunderstood. Silicone rubber does not function as a water vapour barrier akin to hermetic packaging; indeed, it is highly permeable to water (Bian et al., 2020). The critical properties of silicone encapsulation include strong adhesion to surfaces, purity, and low mechanical modulus. Properly applied silicone encapsulation without voids prevents liquid condensation despite rapid saturation with water vapour, thus avoiding ionic current flow and subsequent corrosion (Vanhoestenberghe and Donaldson, 2013; Donaldson, 1973; Sim and Lawson, 1979; Donaldson, , 1991).

Metal enclosures present other practical challenges, such as wireless data and power transmission, high-density interconnections for electrode arrays, sensor interfaces, and maintaining optical transparency for optogenetic implants (Firfilionis et al., 2021; Zaaimi et al., 2022). This research emerged from the CANDO project, that aimed to chronically implant micro-LEDs in cortical tissue (Wellcome Trust WT102037, EPSRC NS/A000026/1) to control neural activity optogenetically. The project necessitated exploring alternative packaging methods to ensure device longevity in the body (Firfilionis et al., 2021; Zaaimi et al., 2022).

2.1 Our previous experimental work

Prior work described the development and validation of the ALTA (*Accelerated Life Testing Apparatus*) for accelerated ageing of

a large number of interdigitated comb samples (IDCs), measured by electrochemical impedance spectroscopy (EIS) (Donaldson et al., 2018). The influence of different passivation layers and encapsulation materials on insulation impedance was then examined by Lamont et al. (2021). In these studies, samples with various passivation and encapsulation combinations were subjected to a biphasic electrical bias (±5 V, corresponding to a field strength of 0.08 V μm^{-1}) at 67 °C. Two groups showed no measurable change in insulation impedance after up to 694 days of exposure: samples passivated with either (1) silicon oxynitride (SiO_xN_y) or (2) silicon oxynitride and silicon carbide on top.

These electrical observations were supported by material analyses, including focused ion beam sectioning with scanning electron microscopy (FIB-SEM), Fourier-transform infrared spectroscopy (FTIR), and X-ray photoelectron spectroscopy (XPS).

Given the predominance of complementary metal–oxide–semiconductor (CMOS) technology for integrated circuits, this new study evaluates whether silicone encapsulated CMOS ICs could reliably support chronic implants lasting beyond 28 days.

The remarkable stability demonstrated herein encouraged a companion study to characterize passivation layer performance and investigated encapsulation breach scenarios, thus reinforcing the potential of silicone encapsulation for advanced bioelectronic implants. This companion paper has been published (Nanbakhsh et al., 2025).

2.2 Review of long-term accelerated ageing studies testing neural implant materials

Our goal is to develop and validate implantable architectures capable of lasting decades, ideally a patient's entire lifetime, to avoid the risks and trauma of repeated surgical interventions. To that end, we arbitrarily focus here on accelerated ageing studies that collected at least 200 days of data under elevated stress conditions. There is no published study performing an accelerated ageing study as long as this.

Troyk et al. developed a comparable silicone architecture to ours, using a silane-enhanced silicone rubber encapsulation strategy for the Intracortical Visual Prosthesis (ICVP). Their approach used DOWSIL 96-083, a silicone adhesive with a silane coupling agent, intended to chemically bond to component surfaces and suppress moisture ingress (The Dow Chemical Company, 2017; White, 1969). Reliability was assessed through aggressive JEDEC-derived accelerated ageing protocols. No failures were observed, even after 250+ days of saline immersion under THB-style (temperature, humidity, bias) ageing conditions (121 °C, 2.35 atm, 100% RH) (Troyk, 2013; Troyk, 2014; Troyk, 2015). These extreme environments offered qualitative evidence of robust encapsulation. However, the absence of multiple ageing temperatures, or any failures, precluded activation energy modelling, and the authors relied on the problematic "Rule of Thumb" heuristic (see the Supplementary Material) to estimate a conservative acceleration factor of ~337×, yielding lifetime projections >200 years at 37 °C. They acknowledged the uncertain nature of such speculative extrapolations. Notably, the sample size was small (n = 4), limiting statistical power. Nevertheless, the study stands out for its unusually long and aggressive test duration, with all implants surviving intact.

Other long-term accelerated ageing studies have evaluated other polymers for neural implant insulation. Polyimide (PI) and liquid crystal polymer (LCP) are the most common alternatives, with LCP showing superior long-term stability. Woods et al. (2018) soaked 61-channel μECoG arrays in saline at 60 °C for up to 487 days and found no LCP failures, while PI degraded earlier. Similarly, Lee et al. (2011) reported monolithic LCP laminates in Phosphate Buffered Saline (PBS) at 75 °C surviving ≥379 days, with failure only at the LCP–LCP bond interface. In contrast, Rubehn and Stieglitz (2010) found PI-insulated structures stable for up to 20 months at 37 °C–60 °C, showing no delamination, while Guljakow and Lang (2023) observed gradual impedance increases but no catastrophic failure over 12 months at 57 °C. Collectively, these results indicate that both PI and LCP exhibit strong medium-to long-term durability under accelerated ageing, with LCP demonstrating particularly promising stability for multi-year use.

We note the growing adoption of accelerated ageing protocols that incorporate reactive oxygen species (ROS) to more closely mimic the inflammatory environment of the foreign body response (Takmakov et al., 2015; Street et al., 2018; Caldwell et al., 2020; Kuliasha and Judy, 2018; Kuliasha and Judy, 2019). While such methods are well-suited to studying oxidative degradation in susceptible materials (such as organic polymers), silicone is known to exhibit strong resistance to oxidative attack (Shit and Shah, 2013). Our previous work compared saline-only accelerated ageing to chronic *in vivo* implantation in rats and found comparable results, suggesting that the silicone encapsulation effectively resists and blocks ROS penetration (Nanbakhsh et al., 2025).

Outside of work specific to implantable neurotechnology, the impact of high humidity on the reliability of integrated circuits has been extensively studied (Vanhoestenberghe and Donaldson, 2013). This is covered in depth in the Supplementary Material.

2.3 Context

Before undertaking the tests we report in this paper, our expectation was that integrated circuits, protected only by silicone encapsulation, would fail by insulation breakdown due to the relatively high field strengths (MV/m) present, as field strength had been established as an important parameter in our review of failure mechanisms (Vanhoestenberghe and Donaldson, 2013).

To validate the encapsulation for a broad range of applications, we considered two use cases for an IC: (i) an IC generating one or several alternating waveforms (typical of LED-drivers or electrical stimulators) where the positive and negative phases would reduce the rate of electrochemical degradation when ionic leakage currents start to flow; (ii) an IC in an implant active all the time, where the power supply voltage is present continuously, creating a "worst-case condition" with a continuous bias ("DC") driving a continued electrochemical reaction. Hence, we tested samples under either a DC or biphasic bias.

Our aim with these tests was to collect data to evaluate whether the device would function for a reasonably long time implanted in a human. We tested samples at three elevated temperatures because if the failure mechanism was the same at all three, this would enable us to extrapolate a sample lifetime at body temperature (see Supplementary Material and Section 5.5).

TABLE 1 Device dimensions and process technology details.

Interdigitated comb dimensions: (See Figure 1E)	Finger width (w)	1 μm
	Gap between fingers (s)	0.5 μm
	Finger length (L)	1.39 mm
	Pitch (λ)	3 μm
	Number of fingers (N)	1,450
Thicknesses in AMS 0.35 μm technology (thin METAL4): (See Figure 1C)	Thickness of METAL1, METAL2, and METAL3	640 nm
	Thickness of METAL4 (top metal)	925 nm
	Thickness of interlayer dielectric	1 μm
	Total passivation thickness	1.6 μm
Width of wall-of-vias (i.e., seal ring)		6 μm
Thickness of silicone encapsulation		~3 mm

Because we did not expect long lifetimes in our accelerated ageing tests, we included, in the design, features that we believed would mitigate the destructive process: a protective metal "shield layer" above the IDC to prevent hydration of the dielectric layer directly above the IDC, and a "double wall-of-vias" to protect the edges of the chip from delamination and lateral water penetration (standard IC layouts already include a seal ring formed of a single wall-of-vias). The sample design and experimental setup are presented in Section 3.1.

2.4 Paper aim

The aim of this paper is to share with the community the remarkable results of the tests that ran over several years. Contrary to our initial expectation, even after four years of immersion, there were no insulation failures; the only IC failures observed were conduction failures (probably) from open-circuits at wire bonds.

Three informative supplements are provided. Supplementary Material 1 provides a background review of the state of the knowledge of encapsulants, interdigitated combs, electro-chemical impedance spectroscopy (EIS), and the principles of accelerated ageing. Supplementary Material 2 describes in detail the experimental setup and EIS analysis using a Modulab XM system for repeatability, including an examination of aliasing and low-frequency electrical noise with representative time-domain and Bode plot data. Supplementary Material 3 presents comprehensive data from electrical and visual observations from all the CMOS IDC samples.

3 Methods

3.1 Sample design

3.1.1 IC technology

CMOS IDCs were fabricated at AMS (Austria Micro Systems AG) in their 0.35 μm CMOS process (C35) with aluminium metallisation and a bilayer passivation of silicon nitride/silicon oxide (see section: "Chemical composition of foundry IC passivation and IMD layers", pg. 3 in (Nanbakhsh et al., 2025))..

3.1.2 Comb design and shield layer

Figure 1 illustrates the horizontal and vertical layouts of the samples. The IDC aluminium metallisation is in the METAL3 layer (typical thickness: 640 nm). Importantly, there is a rectangle of metal in METAL4 (typical thickness: 925 nm), called the Shield, covering the IDC. This was included in the design to protect the active area should the passivation layers become hydrated and degrade. The AMS design rules require regular holes through any metal layer; these are visible in the shield layer in Figures 1A,B. The Shield is therefore perforated. Electrically, it is connected to the substrate, as well as to its own bond pad so its potential is determined.

The IDC, shield and bond pads are surrounded by a rectangular "seal ring". There is also a second seal ring around the edge of the IC, that encompasses additional test structures (irrelevant to the experiment). The seal ring is a standard structure of rectangular metal and polysilicon tracks at all levels, joined vertically by a dense array of metal vias (Figure 1C). We included this "wall-of-vias" to prevent delamination and lateral water penetration, strengthening the structure by the vertical metal bonding, and forming the connection to the p-substrate through a rectangular p + diffusion (Jeng et al., 2008). The final etch which opens windows over the bond pads is applied also around the outside of the seal ring and this penetrates through the passivation layers and some of the inter-layer dielectric (Figure 1C). The wall-of-vias may therefore also prevent cracks propagating from the diced edge into the active area of the chip.

3.2 Sample preparation

3.2.1 Ceramic adaptor fabrication

Ceramic adaptors were made by printing thick film Pt-Au pads and tracks (ESL 5837 G) on ceramic substrates (*Coortek* 96% alumina ADS96R), with overglaze (ESL 4026) over the tracks.

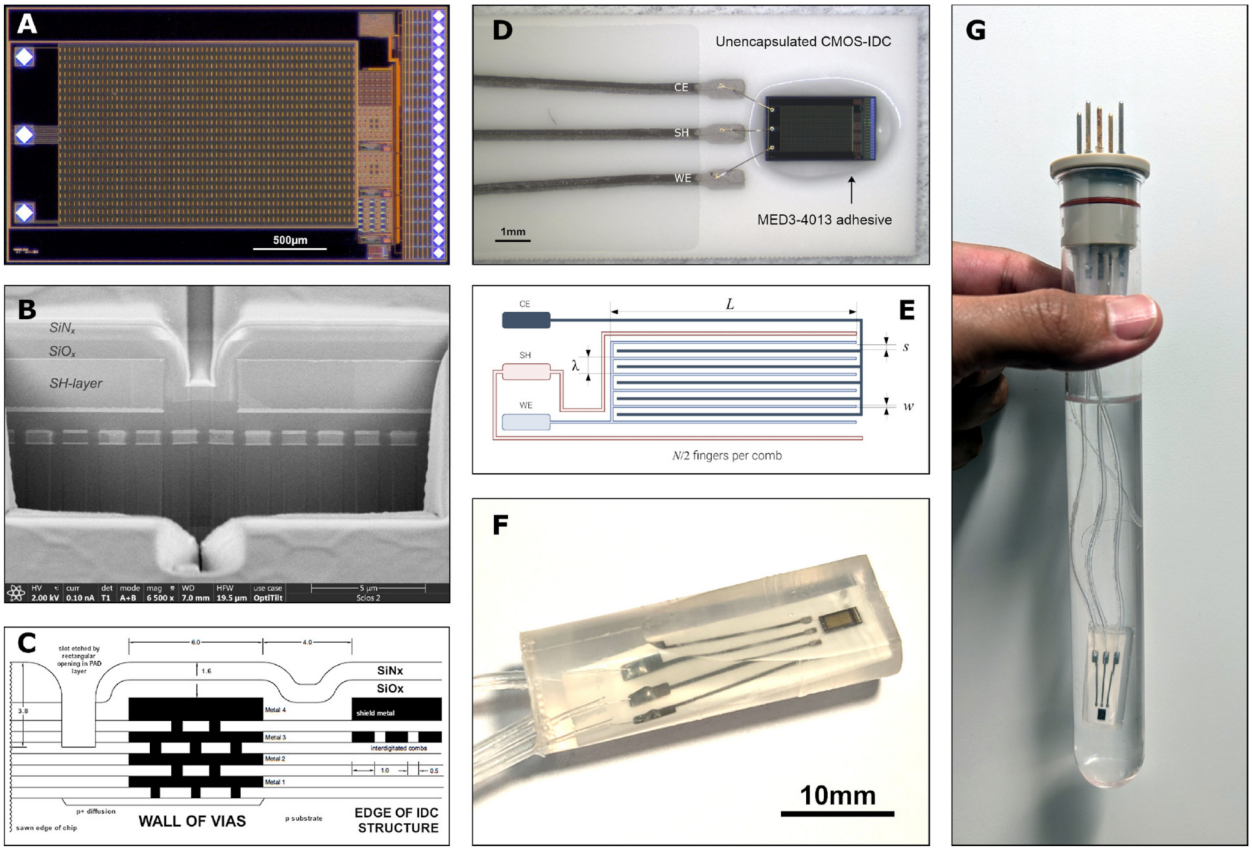

FIGURE 1
Test IC detail: **(A)** Optical photograph of test IC, showing the extent of the perforated shield metal, with bond pads to the left, surrounded by a rectangular "seal ring." Outside that, on the right, are electrical test structures, and on the outside edge is a second seal ring; **(B)** SEM image of a FIB cross-section showing regular perforations in the shield (SH) layer of an IC (METAL 4); beneath is the IDC structure (METAL 3). This chip was fabricated using a different process from that used for the samples presented in this study and features a substantially thicker top metal layer (~3 µm vs. 0.93 µm). Included here for illustrative purposes only; **(C)** Vertical layout of the IC, showing the various metal and dielectric layers, to scale; **(D)** IC bonded on ceramic adapter with MED-4013 silicone, gold wire bonds to the adaptor pads, and overglaze over the Au/Pt tracks; **(E)** Diagram of IDC layout on METAL 3 (see Table 1). SH pad and tracks connected to METAL4; **(F)** Adaptor with IC and wires, encapsulated in MED-6015. Note that this is a photo of an aged sample, the encapsulation has been cut to help visual observation after ageing; and **(G)** Encapsulated device immersed in PBS in a test tube with three wires connected to the bung. Fourth and fifth wires, connecting two depth electrodes to the bung, are also visible.

Teflon-insulated stainless steel wires (75 µm thick) were soldered (*Hydro-X Multicore* SnPb 60/40) onto the Pt-Au pads.

The adapters were then cleaned by sonication in a solution of 97 wt% deionised water +2.5 wt% Na_3PO_4 + 0.5 wt% multi-purpose detergent (Teepol^{TM}), then acetone (99.8%, Sigma Aldrich), then iso-propanol (99.5%, Fisher Scientific) and then DI water (15MΩ cm), for 5 min each.

3.2.2 Die attach and wire bonding

The chip was glued on the adaptor with *Nusil* MED-4013 and cured at 150 °C. Electrical connection between the two components was achieved with wire-bonding using 30 ± m diameter gold wire, see Figure 1D (K&S 4524 Ball Bonder, Kulicke & Soffa Ltd., PA, USA).

3.2.3 Sample washing

Samples were then cleaned in an ultrasonic bath as follows: 1 min in acetone, 1 min in IPA, then 1 min in deionised water, then blown dried with nitrogen gas and further dried at 70 °C for at least 2 h.

3.2.4 Silicone encapsulation

Prior to encapsulation, the samples were held in a *Diener Zepto* Plasma Unit with air plasma for 10 min (4 mBar, 100 W) then immediately encapsulated with MED-6015 (within 5 min). Part A and B were mixed using a *SpeedMixer* at 2,500 rpm for 5 min as the plasma surface activation was occurring. The silicone rubber was then cast round the CMOS chip and the ceramic adaptor, including the solder joint to the stainless steel wire, in a cylindrical PTFE mould. A vacuum centrifuge was used to remove bubbles and de-gas (Donaldson and Sayer, 1975) before curing at 150 °C (room air, atmospheric pressure) for 15 min; see Figure 1F.

3.2.5 IDC to bung connection

After encapsulation, the stainless steel wires from the adapters were soldered to the pins in the test tube bung, two depth electrodes

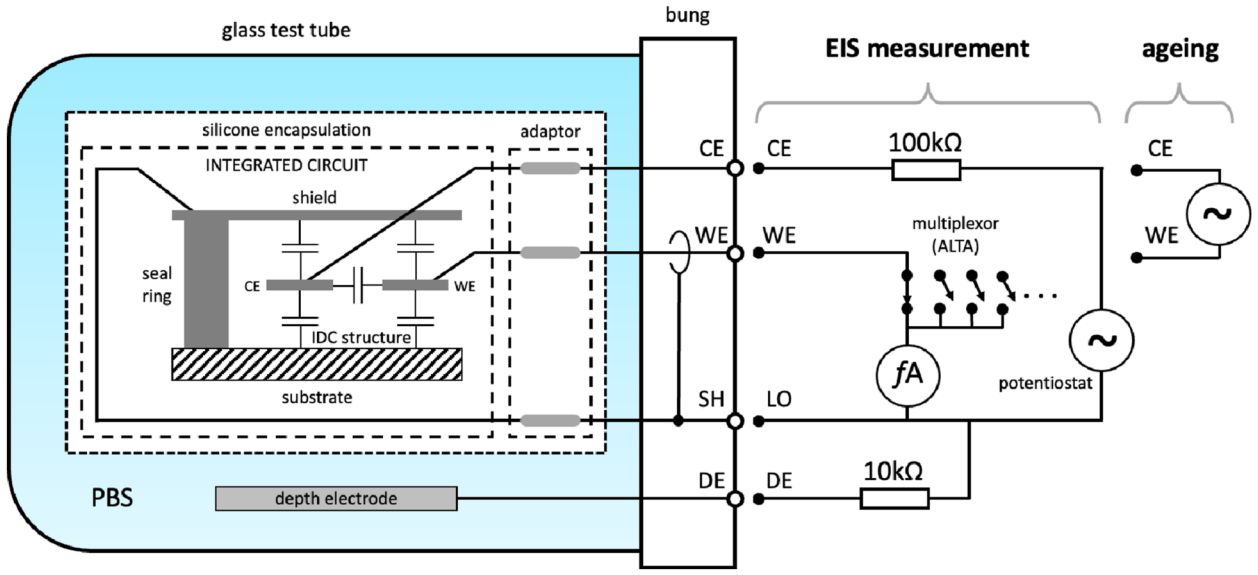

FIGURE 2
Schematic of one sample: the passivation is represented as capacitances between the substrate, the two combs, and the shield (SH). The three bond pads are marked CE, WE and SH. During impedance measurements, connections are made from the source voltage (potentiostat) to CE and a femtoammeter with WE guarded, as shown. During this measurement, WE and SH are at approximately the same potential. The potential of the PBS is defined by connecting the DE (depth electrode) to SH through a 10 kΩ resistor. Most of the time, the ageing voltage is applied between CE and WE with SH floating. Because of the capacitances of the IDC structure, in this situation, while no deterioration has occurred, the potential at SH is approximately mid-way between CE and WE. When the ageing voltage is DC, positive connection is to CE. See (Donaldson et al., 2018) for further apparatus detail.

were also soldered to two other pins on the bung, and the pins and base of the bungs were encapsulated in *Dow Corning*® 3140 RTV silicone.

3.2.6 Pre-ageing characterisation

After manufacture, every sample was visually inspected and photographed (low magnification) for obvious signs of poor assembly, then each was put in an empty test tube. With the sample dry and at room temperature, EIS data (see Section 3.3) was then collected, from 100 kHz down to 100 mHz to check that the ICs were correctly connected (no short nor open-circuit). PBS (Sigma-Aldrich) was then poured into the tube, immersing the sample (Figure 1G). EIS measurement was done again at room temperature (on immersion day), from 100 kHz down to 100 mHz, then the tube was placed in the heated tank.

3.3 EIS setup

The experiments reported in this paper were performed using the ALTA, a dedicated system that has been described in detail (Donaldson et al., 2018).

EIS is performed using a Modulab XM system in a two-electrode setup (see Supplementary Material), applying a sinusoidal voltage between the Counter Electrode (CE) and the Working Electrode (WE) terminals, whilst measuring the current flowing into the WE terminal. There is also a connection from LO to the Shield, to prevent leakage currents not at the IDC from flowing through the femtoammeter (Donaldson et al., 2018). The shield comprises: cable sheaths, tracks on the ALTA modules, a tube around the WE pin at the bung, a track on the adaptor and the metal above and below the IDCs in the CMOS chip. More detail of the apparatus and EIS analysis is presented in Supplementary Material 2.

Figure 2 shows diagrammatically one CMOS IDC sample, connected via its adaptor to the feedthrough pins on the test tube bung. Outside the tube, the multiplexing module is represented with the femtoammeter and the potentiostat. Because the impedance of the femtoammeter is relatively small compared to the insulation being measured, the potential of WE is close to LO, so the impedance being measured is from the CE comb to the WE comb, the shield metal above, and the substrate below. Because the shield metal layer and the substrate are grounded on the chip (see Section 3.1.2) during EIS measurements, the electric field is confined between these layers and will not extend into and beyond the passivation layers. Therefore, the EIS data will not be sensitive to encapsulant delamination or water condensation on the passivation. The data captures only the state (stability or degradation) of the IC metal and interlayer dielectric.

For the data reported in this paper, the EIS measurements were taken by applying a 50 mV RMS sinewave with frequency sweep from 100 kHz down to 0.01 Hz. This is a field strength of 140 kV/m RMS, applied across the SiO_x interlayer dielectric (ILD) between the aluminium combs. There is a similar vertical field strength between METAL3 and METAL4, and between METAL3 and METAL2.

The IDCs have a capacitance of about 150 pF compared to about 6 pF for the ALTA with no IDC connected, as seen in the control samples. Any water that penetrates the sample and bridges the IDCs will appear as a shunt resistance (or perhaps constant phase element) apparent at the low frequency end of the spectrum.

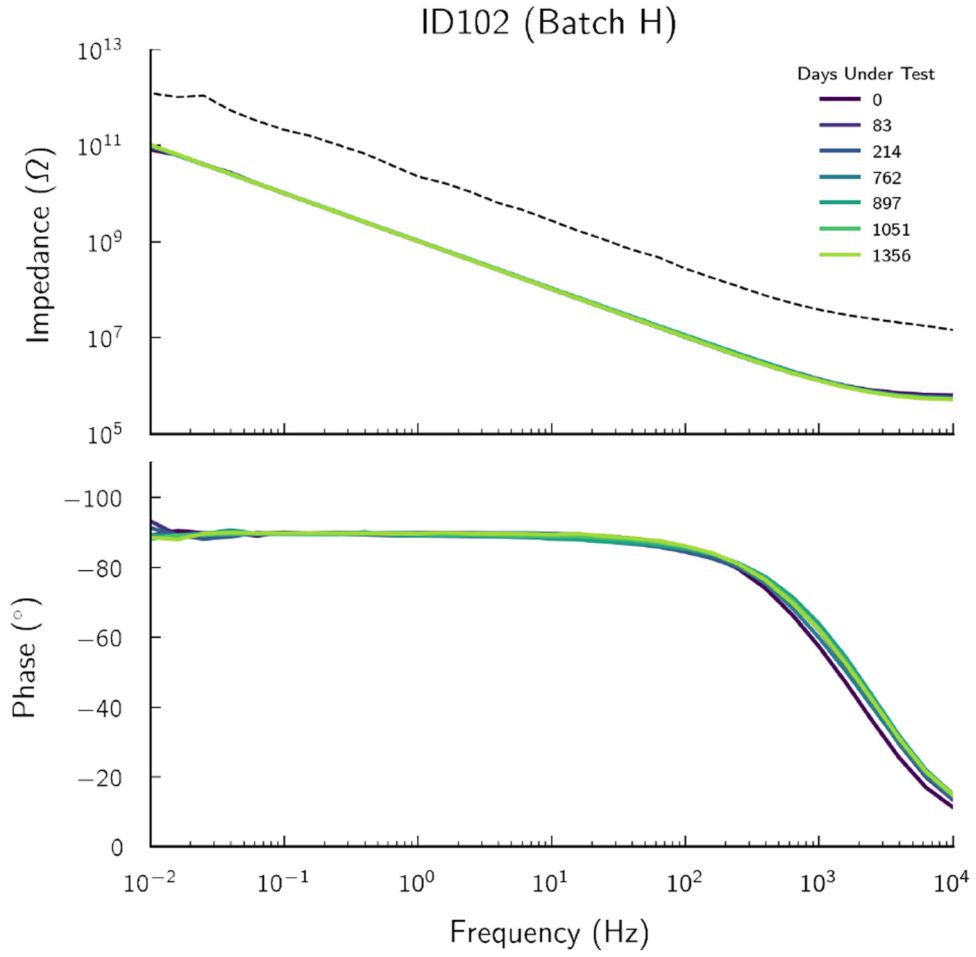

FIGURE 3
A representative set of stable EIS plots from one sample, ID102 (Batch H), showing a characteristic capacitive response across seven time points; the dashed black line is a data point from a control sample, presented for comparison.

Samples without deterioration should have an EIS spectra characteristic of a ~150 pF capacitor from the lowest frequency (10 mHz) up to about 100 Hz where the magnitude approaches a plateau and the phase changes from −90° to 0°, as shown in Figure 3. The plateau resistance would be 100 kΩ if there were only one sample present, but we showed that with several samples connected to the module, the resistance increases proportionally to the number of other samples, giving values close to 1 MΩ (see Equation 8 in (Donaldson et al., 2018)). Therefore, we define insulation failures as a drop in EIS magnitudes of 10% from that of the stable spectrum, as read at 10 mHz (the lowest frequency at which EIS data is acquired).

At high frequencies ($\gg$10 kHz), the RC model exhibits inductive behaviour, with increasing impedance magnitude. This behaviour also depends on the capacitances in other samples in the module.

3.4 Experimental conditions and batch descriptions

We performed tests on 4 batches each containing 10 to 12 samples. For continuity between previous publications from the ALTA experiments (Lamont et al., 2021) we used a unique label for each batch. Hence, we refer in this paper to Batches G, H, I, and J. All samples in these batches are made from the same design of CMOS IDC (Section 3.1), prepared as described in Section 3.2. As shown in Figure Figure 1G, the samples were immersed in PBS, each in their own test tube held at three different temperatures: 47 °C (Batch I), 67 °C (Batches G and H) or 87 °C (Batch J). The PBS was prepared in a cleanroom from deionised water and PBS tablets (Sigma Aldrich).

Each batch comprised a maximum of 12 samples (see Table 2), a control "sample", and one empty channel. Each sample is given a unique ID number. Control "samples" are test tubes, filled with PBS and with depth electrodes connected to a bung (with all bung connections encapsulated) but with neither an IDC nor a ceramic adaptor. The bung is connected to a channel of the ALTA, enabling the collection of data to monitor background noise. The empty channels had no connection to the ALTA, providing information on the sources of interference.

The samples were subjected to an ageing voltage between the CE and WE, i.e., between the two interdigitated combs (see Figure 2), with the shield and depth electrode left floating during ageing (Donaldson et al., 2018). In Batches H, I, and J, the bias

TABLE 2 Summary of batches & experimental conditions.

Condition	G	H	I	J
PBS temperature	67 °C	67 °C	47 °C	87 °C
Ageing voltage	± 5 V	5 VDC	5 VDC	5 VDC
Number of samples	10	11	12	12
Max duration (days)	1,286	1,419	1,587	1,582

was a continuous 5VDC voltage, whilst in Batch G the bias was a 500 Hz biphasic waveform: +5 V, then 0 V, -5 V and back to 0 V, each for 25% of the period. The bias, whether biphasic or DC, was applied continually, interrupted only for the EIS data collection.

An EIS spectrum of each sample in a batch was recorded daily for the first five days, then once a week for the following 3 weeks, then monthly for the duration of the experiment. This ensured that the samples are under bias for the majority of the experiment and also that infant failures may be captured.

When EIS data indicated a failure of the sample (either a 10% or larger drop in impedance magnitude at 10 mHz, or an open-circuit behaviour, see Sections 4.1, 4.2), it was taken out of the ALTA, placed (still in the test tube) in a small separate Faraday cage and characterised at room temperature by measuring the EIS between WE and CE as well as EIS between the Shield and a depth electrode. The sample was then dried and photographed, still encapsulated, before any more destructive investigation.

This experiment was affected by the COVID-19 pandemic. During this period, the samples remained immersed in PBS, at room temperature, without any applied bias. No EIS data was collected. Ageing is considered interrupted during this period, i.e., the number of ageing days was not incremented. All periods reported in this paper exclude the days of the interruption. Batch G was off for 208 days, Batches H and I were off for 209 days and Batch J was off for 210 days.

3.5 Statistical failure analysis

Life-testing results were analysed using Weibull statistical methods, as they are well established parametric methods for survival analysis, that can handle right-censorship of data. Failures were classified based on their relevance to the failure mechanism studied (see Table 3). Samples removed from the experiment due to causes not related to the failure mechanism under study are "right-censored": they are counted as surviving up to the day of removal, but their removal is not categorised as a failure. Weibull analysis requires a minimum of two failures. When this condition was met, reliability was quantitatively evaluated using the Weibull distribution, described in Equation 1:

$$F(t) = 1 - e^{-(t/\eta)^{\beta}} \quad (1)$$

where η is the scale parameter (characteristic lifetime) and β is the shape parameter (indicating failure rate dynamics). All Weibull analyses were performed using Matlab (release 2022b).

4 Results

We tested a total of 45 samples under continuous immersion and electrical bias for durations ranging from 3.5 to 4.3 years (Table 2). Due to the large number of samples and the volume of data collected per sample, individual results are not reported here; a comprehensive table of all results is provided in Supplementary Material 3. Instead, we present an overall summary supported by key tables (Tables 3, 4). This is followed by a focused analysis of stable samples showing no measurable change, as well as control samples (Sections 4.1, 4.2). We then describe the observed failure modes, including open circuits, dielectric insulation degradation, and pad corrosion.

Table 4 summarises the visual observations made on samples that remained at the end of the study, categorised by whether changes were detected in their electrochemical impedance spectroscopy (EIS) profiles. Notably, the table highlights the absence of a clear correlation between changes in EIS and various visible alterations, which are explored in detail in the subsequent sections.

4.1 Stable samples

Overall, 40% of the samples in Batch G and 50% in Batch I appeared unaffected by the ageing environment. These samples exhibited no changes in either their impedance spectra or visual appearance. This level of stability is particularly striking given their prolonged exposure, 1,286 days for Batch G and 1,587 days for Batch I, highlighting their exceptional resistance to both electrical degradation and corrosion. Among the remaining samples in these batches, changes were limited to visual alterations only. Tables 3, 4 provide an overview of all faults and failures observed. In Batch G, aside from a single early (infant) failure, no EIS instability was observed. In Batches H and J, 45% and 42% of the samples, respectively, also exhibited only visual changes, while maintaining electrical stability throughout the testing period.

Figure 3 shows a representative stable EIS Bode plot from ID102 (Batch H); both impedance and phase are very stable. Figure 4 shows a pristine ID104 (Batch H) after 1,419 days at 67 °C under 5V DC bias as a representative of a sample with no visual evidence of degradation: no IC pad corrosion, Pt/Au solder pad corrosion, nor silicone delamination is observed.

4.2 Controls

To validate the EIS measurements, a control sample is included in the ALTA for every batch of samples under test. This control consists of an empty tube, prepared in the same way as the sample channels (filled and sealed with a bung), but without a sample: only the two depth electrodes are connected below the bung. For comparison, Figure 3 includes the EIS spectrum of a control sample (ID140, Batch J, test on Day 4) as a black dashed line alongside the data from a stable sample (ID102). The impedance magnitude of a control channel is more than one order of magnitude higher than that of good samples and serves as a benchmark for identifying when a sample has failed as an open-circuit.

TABLE 3 Summary of sample faults and failures. These are of four types: (1) open-circuit failures at wire bonds; (2) intermittent open-circuits; (3) delamination at an adaptor leading to CE-SH leakage; and, (4) leakage currents WE-SH at the bung.

ID	Batch	Fault Day(s)	Retirement day	Fault/Failure mode	Comment
91	G	0	0	Wire bond o/c	Infant failure
103	H	71	71		o/c failure at CE, no delamination
110	H	447	447		o/c failure at CE, no delamination
128	J	2	2		Infant failure
131	J	1,000–1,200	1,582	Intermittent o/c	Recovered after day 1,200; no fault at day 1,582
137	J	0	500		Recovered after day 0; no fault at day 500
138	J	0–7	500		Recovered after day 7; no fault at day 500
132	J	45	45	Delamination at adaptor	CE–SH (~1 MΩ at f = 10 mHz)
106	H	71	71	Bung leak	WE–SH leak (~1 GΩ at f = 10 mHz); probably at bung
108	H	441	441		WE–SH leak at bung
136	J	1,582	1,582		WE–SH leak at bung

TABLE 4 Overview of visual observations of corrosion of the samples remaining at the end of the experiment. The results include both absolute counts and percentages of the total number of samples per batch. What constitutes a stable/unstable EIS or a change in visual condition is defined in Sections 4.2 onwards. See Supplementary Material for full description of conditions.

Category	Condition	G (n = 9)	H (n = 8)	I (n = 12)	J (n = 8)
Stable EIS (n = 31; 84%)	No corrosion observed	4 (44%)	–	6 (50%)	–
	Visible Pb/Sn solder corrosion only	1 (11%)	–	–	–
	Visible Al bond pad corrosion only	3 (33%)	4 (50%)	4 (33%)	–
	Visible solder & bond pad corrosion	1 (11%)	1 (13%)	2 (17%)	5 (62%)
Unstable EIS (n = 6; 16%)	No corrosion observed	–	–	–	–
	Visible Pb/Sn solder corrosion only	–	–	–	3 (38%)
	Visible Al bond pad corrosion only	–	–	–	–
	Visible solder & bond pad corrosion	–	3 (38%)	–	–

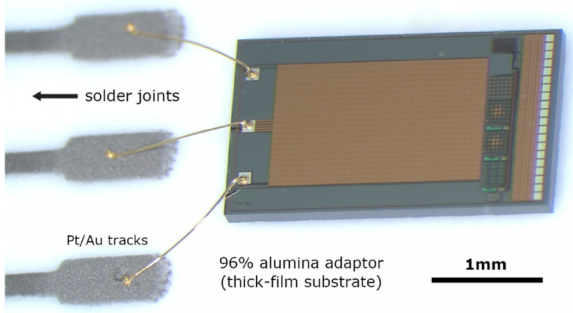

FIGURE 4
A representative visually pristine sample post-ageing (image taken through transparent MED-6015 silicone): ID104 (Batch H) after 1,419 days at 67 °C under 5V DC bias, no IC pad corrosion nor Pt/Au pad silicone delamination.

4.3 Failed samples

The regular EIS data identified permanent failures or temporary faults (including equipment faults) in 11 of the 45 samples, as summarised in Table 3. Four were open-circuit wire bonds but two of these occurred on Day 0 or Day 2 and we consider these infant failures due to poor bonding rather than due to ageing. We classified three as intermittent open-circuits (all in Batch J). One sample (ID132) showed an increase in the EIS impedance as measured between WE and CE (Figure 5). Upon further investigation, we measured, outside the ALTA, an impedance of ~1 MΩ at 10 mHz, between the CE and SH. On visual observation, silicone delamination was observed both at the Pt/Au pads on the ceramic adaptor, where the area delaminated was shorting the CE and SH. Delamination was also observed at the wire-bond pads on the IC, however this did not short the pads and the failure is recorded as delamination at the adaptor. Finally, three samples developed leakages from SH to WE, two definitely at the bung and one (ID106), probably at the bung.

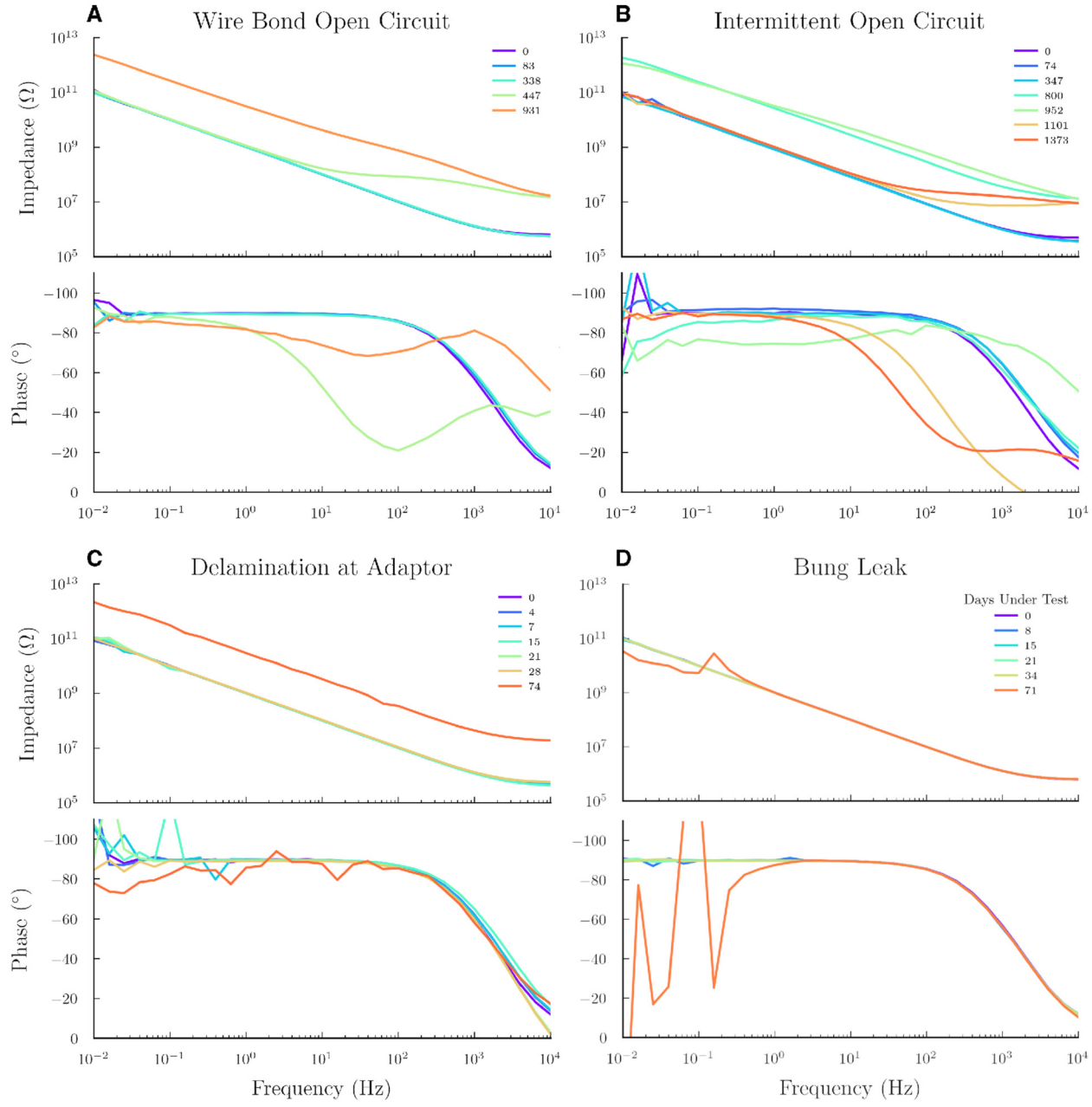

FIGURE 5
Representative EIS spectra of the four modes of failure/fault observed in the IDC samples. **(A)** Wire bond open circuit failure in ID110 (Batch H) at Day 447. **(B)** Intermittent wire bond open circuit failure in ID131 (Batch J). **(C)** Delamination between the silicone rubber and the Pt/Au causing a leakage between the CE and SH Pt/Au pads on the ceramic adaptor in ID132 (Batch J); the leakage causes an apparent increase in the EIS impedance between CE and WE (see Supplementary Material). **(D)** A leak at the bung between SH and WE in ID106 (Batch H) (see Supplementary Material).

In Section 3.3, we described how failure of the passivation layer by hydration should lead to a decrease in the impedance across the spectrum. We did not observe this in any sample; again we emphasise, we observed no insulation failures in any sample over 3.5–4.3 years of ageing.

4.4 Reliability statistics

Table 3 provides an overview of the sample failures and faults observed during the study. For the purpose of studying the underwater reliability of silicon ICs encapsulated in silicone rubber, some of the faults are considered as unrelated to the immersion and failure mechanisms studied, and those samples are right-censored in the reliability analysis. This includes the infant failures at day 0 (Batch G) and day 2 (Batch J) and the three failures attributed to leaks at the bung (Batch H, days 71 and 441, and Batch J, day 1,582). The rest are interconnection failures. Since our samples were so stable that we did not observe any insulation failures, we are categorising the interconnection failures as failures (hence the failure mode

TABLE 5 Corrosion of Al bonds pads and Pb/Sn solder joints by pad and batch. For bond pads, under microscopic examination, corrosion was categorised into: none (=0), slight (=1), extensive (=2) or total (=3). These were added for each group and sum expressed as a percentage, where 100% would mean all pads were totally corroded, and 0%, no pads corroded. Similarly, for solder joints, pads were sorted into three categories: bright (=0), grey (=1) or black (=2). These were added for each group and sum expressed as a percentage, where 100% would mean all pads were black, and 0%, all pads were bright.

Batch	Pad	IC bond pad	Solder joint
G (67 °C)	CE	30%	11%
	SH	0%	6%
	WE	19%	6%
H (67 °C)	CE	54%	0%
	SH	13%	6%
	WE	25%	0%
I (47 °C)	CE	19%	4%
	SH	19%	8%
	WE	28%	8%
J (87 °C)	CE	79%	63%
	SH	79%	75%
	WE	83%	38%

studied in the survival analysis is no longer insulation failure). All non-failed samples are also entered as right-censored at the completion of the study.

Since there are no failures in Batch I, and no relevant failures in Batch G, Weibull analysis cannot be used to calculate survival data for those batches.

For Batches H and J, the Weibull parameters (η is the scale parameter and β the shape) were η = 51.5 years with β = 0.56 in Batch H (67 °C) and η = 12.5 years with β = 0.74 in Batch J (87 °C).

4.5 Solder and Al bond pad corrosion

We completed a visual inspection of all the samples still under test after 3.5–4.3 years (i.e., all the samples except the eight samples that had been removed for further analysis earlier during the experiment). An overview of the outcome of the visual observations is included in Table 4, with details of which of the CE, WE or SH pad was corroded presented in Table 5. The full analysis is in Supplementary Table S4. Figure 7A shows a shiny Pb/Sn solder bond even after 1286 days of ageing at 67°C.

27 samples, representing 40% of Batch G, 72% of H (100% of the samples remaining at the end of the study), 50% in I, and 67% in J (100% of the samples remaining at the end of the study) had visible corrosion of the Al bond pad or the solder joint (see Figure 6). Of these, 21 samples had visual changes and no change in EIS. Comparatively, no samples had changes in EIS without visual changes.

There were no visible changes to the thick-film pads or tracks of the adaptors. On the adaptors, the tracks are coated with an overglaze layer, only the pads are exposed, hence they may appear lighter on the photographs.

Looking specifically at the Al bond pad corrosion, visible corrosion covered a wider area of the Al bond pads in Batch J samples (87 °C), as seen in Figure 6B). In Batch G (biphasic bias), the corrosion covered less than 50% of the pads except in the only sample that also showed EIS changes (ID093, see Supplementary Material 2). In Batch H (DC bias) all samples with corroded bond pads had corrosion on either CE or WE or both, and three of them also had minor signs of corrosion on the SH pad. A similar trend was observed in Batch I (also DC bias): all samples with corroded bond pads have corrosion on pads CE or WE or both, and three also have signs of corrosion on the SH pad. In Batch J (also DC bias) however, corrosion of the SH pad was present in all samples with corroded pads, and in all of them it was the most corroded pad. In one sample (ID134, with EIS change), corrosion was also observed along the track leading to the SH bond pad.

4.6 Changes in the silicone

The silicone remained optically clear in Batches G (47 °C), H (47 °C), and I (67 °C). In Batch J, immersed at 87 °C, there was a yellowing of the silicone rubber in 5 of the 8 samples available for visual observation (Figure 7B).

Also, only in Batch J, we also observed cracks in the rubber, which we called “shear voids”. These were planar and oblong, usually steeply-inclined to nearby rigid surfaces, but not extending to touch the surface. The silicone rubber appears to be cleaving to relieve stress (see Figures 7C,F–H). This was observed on 7 of the 8 surviving Batch J samples, and were accompanied by changes in EIS in samples 129, 130, 131, and 134, where the voids occurred over the IDC area as shown in Figure 7F.

Batch J was also the only batch where we observed signs of delamination of the encapsulant over the thick-film pads with the wire bonds to the IC (See Table 6 and Figure 7D). This was observed in five samples: ID130 (WE); ID139 (CE); ID135 (CE and WE); and ID132 & ID136 (CE, WE, and SH). Only two samples showed corresponding changes in EIS: ID130, which also exhibited voids above the IDC surface, and ID132, where delamination extended between pads, resulting in a significant leakage impedance between CE and SH of approximately ~1 MΩ at f = 10 mHz. We did not expect much adhesion to the thick-film Pt-Au but leakage currents should be prevented if adhesion remains to the alumina substrate. We do not know why it failed in this sample specifically, but the stress due to thermal expansion was greatest in this batch.

Figure 7I shows a single instance of process failure leading to poor encapsulation (ID094, Batch G, 1,286 days at 67°C) leading to a worm-like void beneath the wire bonds. The EIS remained unaffected.

5 Discussion

5.1 No insulation failures on IDCs

The most obvious failure mode of electronic devices operating in a wet environment is insulation failure as water enters the structure

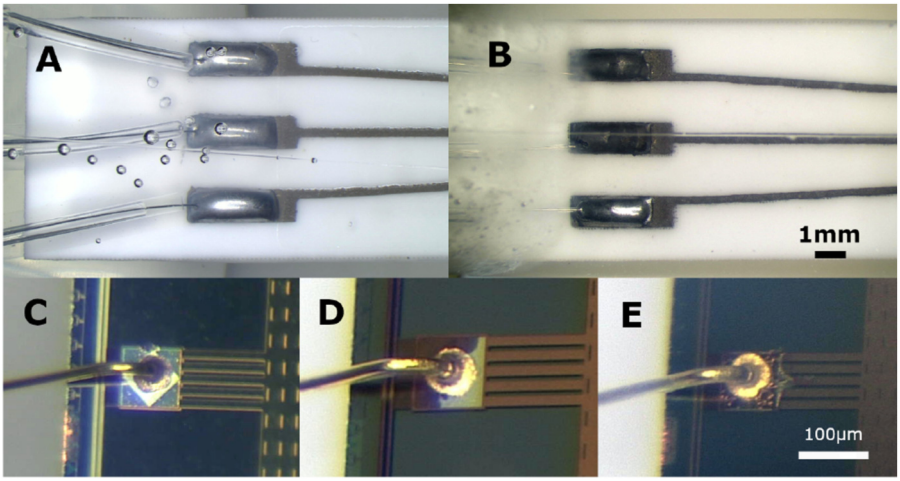

FIGURE 6
Examples of post-ageing corrosion of solder pads and bond pads; structures within clear silicone. **(A)** ID086, Batch G, 1,286 days, classed as "no visual changes" (note that the bubbles visible are not in contact with any conductive surfaces and hence do not affect the encapsulation efficacy); **(B)** ID130, Batch J, 1,582 days, where the solder appears black at the CE and SH connection, whilst still bright at the WE; **(C)** ID117, Batch I, 1,587 days, SH bond pad is bright, no corrosion; **(D)** ID118, Batch I, 1,587 days, slight SH bond pad corrosion; **(E)** ID139, Batch J, 1,582 days, total SH bond pad corrosion (this did not appear to affect the EIS spectrum).

and forms conducting pathways. We tested IDCs immersed in saline held at three temperatures (47 °C, 67 °C and 87 °C) and two voltage biases (5 V DC or ± 5 V biphasic) for 3.5–4.3 years and we did not detect, in any of the samples, any reduction in their impedance due to insulation failure ($|Z| \approx 10^{11}\ \Omega$ at $f = 10$ mHz; see Figure 3 for an example of an unfailed sample). Thus, there was no significant water ingress in any sample. As described in Section 3.1, we designed the test chip with a shield layer (a continuous but perforated metal layer deposited above the IDC passivation layer) and also included the wall-of-vias to reduce lateral penetration, but still, as water will diffuse through the silicone encapsulant, we expected that it would penetrate the chip if there were any crevices, pores or pinholes, larger than water molecules.

The fact that we did not observe any such reduction in impedance means that there are no crevices, or at least, that they have no functional effect even after so many years. The AMS chips we tested, with bilayer silicon oxide/silicon nitride passivation, are effectively flawless. Nevertheless, when exposed to an ionic environment (without encapsulation) the silicon nitride layer does dissolve. Our companion paper reports dissolution rates in PBS of 120 nm/month for ICs from one foundry and 22 nm/month for ICs from another (Nanbakhsh et al., 2025). This shows that the silicone encapsulant prevents dissolution of the passivation.

These observations are supported by earlier work, such as that of Osenbach who tested IDC chips (which we assume he produced in his own lab) encapsulated with a silicone described as "Dow Corning RTV" aged in deionized water at 96 °C (Osenbach, 1993). He found that a minority (16%) failed after 250 h but there were then no further failures up to 700 h (when the experiment was terminated). In a second lot, he intentionally produced voids in the encapsulant by shaking the container to introduce bubbles before application. Consequently, the number of failures rose to 63% after 250 h, with no additional failures observed up to the end of the experiment (1,000 h). Failure occurred because the passivation layer dissolved where the voids in the rubber were touching the IC surface, exposing the underlying metal. 250 h would be the time taken to dissolve the passivation layer in Osenbach's samples.

Given these results, we suggest that there are three reasons why we have not observed electrical insulation failures in our IDCs. The first is the presence of the shield layer, so that if the passivation layers dissolved, the IDC tracks would not immediately be exposed; the aluminium shield and the underlying dielectric would also have to dissolve before the IDC were exposed. The second reason is the remarkable insolubility of modern passivation layers, so that, if there is delamination at the interface, it will take years for the passivation layers to dissolve. Finally, given our specific surface preparation, the MED-6015 silicone rubber encapsulation appears to have excellent adhesion to the passivation layer, with no signs of delamination, even after so many years at elevated temperatures in saline (Donaldson, 1996; Donaldson, 1994).

5.2 Silicones

Nusil MED-6015 was selected primarily for its optical transparency. The CANDO project (Zaaimi et al., 2022), which funded this work, required a transparent and biocompatible micro-LED encapsulant that would not interfere with light transmission essential for optogenetic stimulation of transfected neurons. We previously compared its performance with MED3-4013 (Lamont et al., 2021). It is an unfilled 2-part liquid silicone rubber that cures via platinum-catalysed hydrosilylation at 150 °C. It is not advertised as an adhesive and yet has demonstrated remarkable water-resistant adhesion to the IC surface. The vendor (Polymer Systems Technology Ltd.) recommended that we use MED-163 primer to bond to gold, but we doubted that we could apply it as an aerosol consistently from batch to batch, hence our choice not to use it. For comparison, the WFMA device (described later) used Dow 96-083 (self-priming). The P. E. K. Donaldson work used Dow Corning

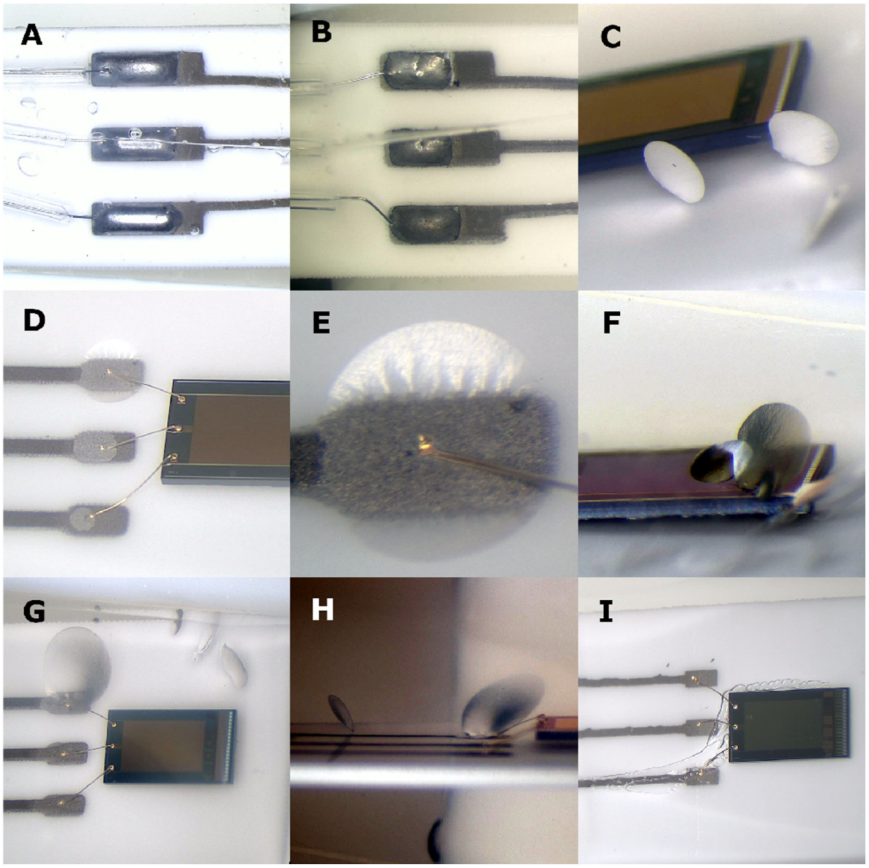

FIGURE 7
Various rare defects in the encapsulation. **(A)** Clear silicone (ID085, Batch G, 1,286 days at 67 °C); **(B)** pronounced silicone yellowing (ID129, Batch J, 1,582 days at 87 °C); **(C)** cracks in the silicone bulk (ID129, Batch J); **(D)** silicone delamination over the Pt/Au bond pads (ID136, Batch J); **(E)** zoom shot of same sample (ID136) over the CE pad showing "blistering" behaviour; **(F)** "shear voids" or cracks directly above IDC, at the corner of the chip (ID130, Batch J); **(G)** crack intersecting with Pt/Au pad delamination (ID139, Batch J); **(H)** oblique view of same sample (ID139) showing crack; **(I)** single instance of worm-like void beneath the wire bonds, which was due to poor encapsulation, (ID094, Batch G, 1,286 days at 67 °C) but the EIS remained unaffected.

3140 and 734 (Donaldson, 1973; Donaldson, , 1991; Donaldson and Sayer, 1975; Donaldson, 1996; Donaldson, 1994; Donaldson, 1976; Donaldson and Aylett, 1995; Donaldson, 1995; Donaldson and Sayer, 1977). Similarly, the work in our companion paper (Nanbakhsh et al., 2025) used room-temperature cured Dow Corning 3140 (*in vitro* ageing tests) and MED2-4213 (*in vivo* ageing tests). Much work published in biomedical applications written as "PDMS" implies Sylgard-184, which is not an adhesive (Bachoux et al., 2024; Park et al., 2018; Bernardi et al., 2017; Andersen and Schouenborg, 2023; del Carmen Fuentes et al., 2017).

We suspect that the MED-6015 adhesion is a chemical bond to the surface enhanced by our air plasma treatment, but at the present we do not know definitively.

5.3 Failures and faults

Whilst no changes indicative of insulation failure at the IDCs were observed, eleven samples failed or were faulty, as listed in Table 3. Seven were open-circuits: two infant wire bond failures, two open-circuits at the CE connection of uncertain cause (no signs of degradation were visible under the optical microscope), and three intermittent open-circuits. One sample (ID132) delaminated at the adaptor and developed a leakage impedance between CE-SH of ~1 MΩ at f = 10 mHz, making the apparent CE-WE impedance abnormally high (Figure 5C). Three samples developed leaks at the bung between the WE pin and the surrounding shield tube (see Figures 5C,D in (Donaldson et al., 2012)).

This section will discuss these various failures in subsections on: apparatus, corrosion & silicone-related phenomena.

5.3.1 Apparatus fault: bung leaks

The impedances measured in this experiment are extremely high compared to the insulation likely to be required in typical implanted medical devices. For example, the leak at the bung on ID106 was 1 GΩ. These leaks appeared after periods of 71–1,582 days in the apparatus, with the test tube containing the sample continuously immersed in water at 67 °C or 87 °C. In future, it might be possible to find a better adhesive for joining the silicone sleeves that surround the WE wire and pin at the bung, in order to prevent this fault. Certainly, these joints need to be very carefully inspected before using them in the apparatus.

5.3.2 Interconnection failures

Interconnection failure at wire bonds is a known weakness of implanted devices; we have previously reported on gold wire bond failure on aluminium pads (Lamont et al., 2021; Nanbakhsh et al., 2025). The presence of the silicone encapsulant makes it difficult to check whether the wire bonds are still firmly attached to the bond pad or merely touching. In the absence of any other signs of degradation, it is likely that all open-circuit samples (whether infant or gradual) failed at a wire bond. The infant failures indicate that our bonding process was sub-optimal, which is not surprising as we only bond ICs occasionally. Commercial packaging houses would probably have made more reliable joints.

The silicone encapsulant prevents dissolution of passivation by remaining bonded to the surface, but it does not prevent corrosion of the bond pads or the solder. The visible change in these surfaces is dependent on the temperature (see Figure 6). The fact that this corrosion is occurring on the bond pads probably means that adhesion to the encapsulant is lost and therefore that there will be a film of moisture present at the interface. The welded joint between aluminium and gold forms inter-metallic compounds which are brittle but conductive, and grow as the metal atoms diffuse, perhaps forming *Kirkendall voids* due to the differing densities of the various compounds. At high temperatures, this may cause joint failures (open-circuit) even when dry. The presence of water at the joint surface can cause failure at lower temperatures if there is halogen contamination, which would probably be chloride from the PBS or fluoride from residual foundry etchants in this case (Harman, 2010). The various intermetallic compounds also have different galvanic potentials, so are likely to corrode where two or more are exposed to the water film. There is likely also to be a water film at the encapsulant-gold interface because adhesion to gold is generally poor, so the water film may well bridge the Al-Au joint, leading to galvanic corrosion with the aluminium being oxidised, the potential difference being about 1.3V (Griffin et al., 1994). These considerations suggest the need for a better design of joint than the gold ball on the aluminium pad. One possibility is to gold-plate the Al pads so that the weld is Au-Au, avoiding intermetallics (Harman, 2010). Because more of the surface is now gold, the extent of the liquid film may be greater, but the argument in favour is that it is all gold so will not corrode. However, if a small area of Al remains exposed, perhaps at the edge of the pad, corrosion will be rapid because of the large area for reduction on the gold with high current density at the aluminium. Alternatively, using Al wire on the Al pads would also avoid intermetallics, and improve adhesion (because silicones adhere well to Al_2O_3 (Donaldson and Aylett, 1995)) but the metal at the pad at the other end of the wire must also be chosen so as not to be vulnerable.

More advanced metallisation stacks are also possible; for example, in the under-bump metallization (UBM) process, which prepares IC pads for solder bumps, a metal stack for aluminium pads can include a titanium-tungsten adhesion layer, followed by a nickel-vanadium barrier layer, finally topped with a copper solder-wettable layer (Arshad et al., 2007).

The Troyk architecture (Troyk, 2017) utilises gold wire bonds to establish connections between their ASICs and ceramic adaptors in their wireless floating micro-wire array (WFMA) device (Frederick et al., 2022). Their device has been implanted in a human volunteer for more than a year as the Intracortical Visual Prosthesis (ICVP) with no reported failures, demonstrating their architecture to be robust (Barry et al., 2024; Jiang et al., 2024; Grant et al., 2024; Barry et al., 2023a; Barry et al., 2023b). Their process involves gold bumping their ASIC pads as a foundry-level process, pre-dicing, prior to gold wire bonding (from personal communication with Troyk; published with permission). Thus, the durability of the interconnections can be attributed to the robustness of the gold–gold bonds. This is visible in Figure 8.

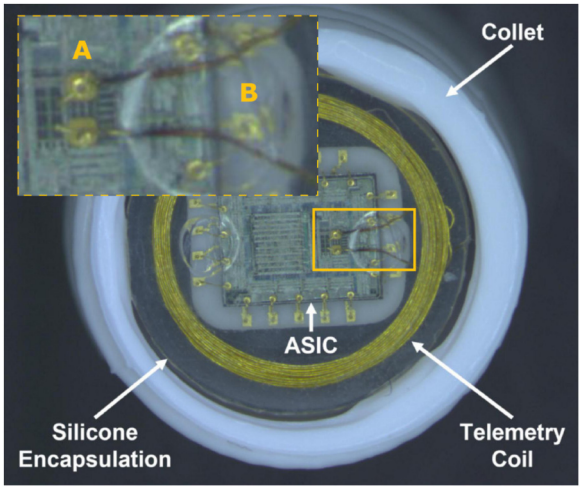

FIGURE 8
The wireless floating micro-wire array (WFMA) device (zoom emphasis ours): **(A)** Indicating where the chip pads appear metallised with gold; **(B)** Indicating the ceramic baseplate has gold tracks. Reproduced from (Frederick et al., 2022), Frontiers in Neuroscience (2022), under CC BY license.

Thus, we conclude that we might have had fewer conduction failures if the wire bonds had been fabricated by a commercial electronics assembly company and if we had gold-bumped the pads. However, for long-term implantable applications, further research is required to ensure the reliability of encapsulated wire bonds and electronic interconnects operating in wet environments. Comparative studies of various metallisation stacks, wire types, and silicone encapsulants under simulated *in vivo* conditions are needed. Ideally, the bond welds should remain stable over time, but also strong adhesion should be maintained between the metal surfaces and the encapsulant.

5.4 Other observations

5.4.1 Cracks in the silicone

This is the first time that cracks in silicone rubber encapsulant have been reported. Although none of them appeared to allow liquid to reach the passivation and cause corrosion, this phenomenon clearly ought to be understood.

The formation of cracks in soft rubbers when placed under triaxial tension was described in 1958 by Gent and Lindley (1959). They found that the stress at which this occurred was proportional to the Young's Modulus for the rubber. Pourmodheji et al. presented a theory which shows that cracks or spherical voids form under these

TABLE 6 Extent of delamination on adaptor pads by batch: none, slight, extensive, or total.

Batch	n	None	Slight	Extens	Total
G (67 °C)	9	6	3	0	0
H (67 °C)	8	8	0	0	0
I (47 °C)	12	12	0	0	0
J (87 °C)	9	4	0	3	2

TABLE 7 Number of cracks in the silicone per sample by batch.

Batch	Bias	n	0	1-5	>5
G (67 °C)	± 5 V	9	9	0	0
H (67 °C)	5 VDC	8	8	0	0
I (47 °C)	5 VDC	12	12	0	0
J (87 °C)	5 VDC	8	1	4	3

conditions, depending on the size of pre-existing defects in the rubber, larger defects favouring cracks. Their results show that for a rubber with a Young's modulus of 10 MPa, which is approximately right, the triaxial stress would need to reach about 50 times atmospheric pressure (5 MPa) to cause cracks, which seems unlikely (Pourmodheji et al., 2018). However, these papers describe the situation where crack propagation occurs soon after loading whereas in our samples, the cracks may have appeared after a long time in hot water, which may be quite different.

P. E. K. Donaldson compared the time-to-failure of dummy implants made with beam lead transistors with silicone encapsulation in several configurations (Donaldson, 1976; Donaldson and Sayer, 1977). He found that the time-to-failure depended on the constraints on the encapsulant: if unconstrained so as to allow changes in volume without large stresses, the devices survived for longer. Thus, thin (a few mm) coatings of ICs should be safe because the encapsulant is not put under stress.

In this experiment, the IDC chips were encapsulated in a mould and once removed, the rubber was free to move perpendicular to the chip surface in order to accommodate volume changes. The mould was made of PTFE, chosen so that the rubber would not adhere to it, but nevertheless, perhaps significant tensile stress was applied as the samples cooled after curing, which led to the cracks immediately or later. However, as shown in Table 7, cracks only appeared in samples from Batch J, strongly suggesting that the high temperature ageing causes cracking, though whether due to the greater thermal expansion causing greater stress, or due to faster structural changes in the polymer (such as loss of unbound oligomers), we cannot say.

Silicone rubber is used in a wide variety of implanted devices, contributing a cumulative experience of its bulk behaviour in response to long-term exposure to body fluid. To the best of our knowledge, cracks as those observed in this study have never been reported (Brindley, 1995). As they are only observed in the highest temperature batch, they appear to be a consequence of the extreme environment, not representative of failure modes likely to occur in use (see Supplementary Material 1, Section 3).

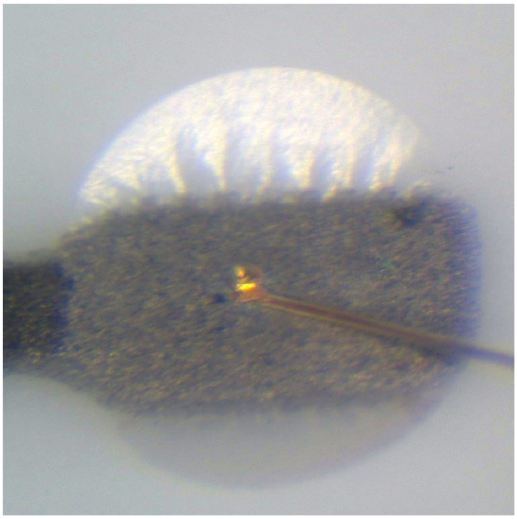

FIGURE 9
The silicone-encapsulated Pt/Au counter electrode (CE) pad on the alumina adaptor of ID136; blister diameter ⌀1 mm.

5.4.2 On adhesion & blistering

Accelerated ageing tests revealed a distinct *blistering* failure mode in ID136 at the counter electrode (CE) pad (see Figures 7D, 9) that deserves further attention. The circular morphology of the blister suggests that the delamination is driven by isotropic internal pressure.

Similar but less circular failures were observed at pads in other samples aged at 87 °C (ID135, ID139) whereas sample ID130 exhibited delamination exclusively at the working electrode (WE) pad. This selective occurrence exclusively at 87 °C highlights a synergistic effect of elevated temperature and DC bias, required to induce the observed encapsulant delamination.

5.4.2.1 Local acidification at the anodic pad

Delamination was most pronounced at anodic (CE) pads under +5V DC bias, implicating electrochemical processes. The anodic reaction ($2H_2O \rightarrow O_2 + 4H^+ + 4e^-$) produces protons ($H^+$) that locally acidify the interface, thus weakening silicone-substrate bonds. Oxygen gas evolution additionally induces mechanical stress, creating the blistering effect observed in ID136. Previous work correlated acidic conditions with reduced silicone adhesion under hydrothermal conditions (Donaldson, 1994) supports this hypothesis.

This was observed over the counter electrode (CE) in ID136 (see Figure 7E). We found that ID136 had failed with a relatively low impedance from WE-SH at the bung. During ageing, SH is usually floating with 5V applied between CE (+) and WE (–). With this bung leak, voltage would appear across CE-SH at the adaptor which would drive electrolysis there at a rate that would depend on delamination between the pads (refer to the circuit diagram Figure 2). Note that blistering of ID136 was therefore probably a double fault, with failures at the bung and on the adaptor, where the blistering occurred.

5.4.2.2 Oxane bonds and hydrolytic equilibrium

A general equation for the condensation reaction of a surface hydroxyl (on some metal M) with a silanol for the formation of an *oxane bond* is shown in Equation 2:

$$\mathrm{M{-}OH + HO{-}Si} \equiv \rightleftharpoons \mathrm{M{-}O{-}Si} \equiv + \mathrm{H_2O} \tag{2}$$

Equation 3 describes a specific case of this, i.e. the bonding of silane coupling agents to silica (Plueddemann, 1991) (or perhaps the passivation of an IC):

$$\begin{aligned} &\equiv \mathrm{Si{-}OH + HO{-}SiR_{\mathit{n}}(OH)_{\mathit{m}}} \rightleftharpoons \\ &\quad \equiv \mathrm{Si{-}O{-}SiR_{\mathit{n}}(OH)_{\mathit{m}} + H_2O} \end{aligned} \tag{3}$$

In this equation, *R* refers to a non-hydrolysable organic group, typically containing a functional moiety (e.g., vinyl, amino, or epoxy) that can form covalent bonds with a broader polymer network.

Our theory is that the silicone (MED-6015) adheres to the surface through some process analogous to that of a silane coupling agent reacting with surface hydroxyl groups (which we induced via air plasma). Silane coupling agents anchor polymers to inorganic substrates through the formation of oxane bonds (M–O–Si), yet these linkages are far from immutable. Even fully covalent siloxane (Si–O–Si) bonds are susceptible to hydrolytic cleavage, reverting to silanols with an activation energy of only 98.7 kJ/mol (Plueddemann, 1991). The propensity for hydrolysis is accentuated by the highly polar nature of the Si–O bond: whereas the Si–C bond possesses roughly 12% ionic character, Si–O is about 50% ionic, and M–O–Si bonds to many metals (e.g., Al, Fe, Ti) are still more ionic. In such ionic, inorganic systems the interfacial chemistry is governed less by kinetics than by reversible equilibria; bond formation and breakage proceed according to concentration-driven equilibrium constants.

Water inevitably permeates the polymer/substrate interface, and its impact varies with the surface chemistry of the particular substrate. Silane coupling agents do *not* exclude this moisture; rather, they preserve adhesion by allowing the interface to cycle through hydrolysis and re-condensation. Oxane bonds formed with silica or glass, for instance, hydrolyse during prolonged immersion but re-form upon drying, evidencing a reversible, quasi-equilibrium condition at the interface. Direct proof of true equilibrium is elusive, yet the collective observations of silanol–siloxane interconversions strongly imply that interfacial bonding is dynamic and concentration-controlled rather than permanently fixed (Plueddemann, 1991).

5.4.2.3 Stable adhesion

Plueddemann outlined three key conditions for favourable siloxane bonding equilibria, i.e., to favour condensation over hydrolysis: (1) maximal initial formation of M–O–Si bonds, (2) a minimal equilibrium concentration of water at the interface, and (3) polymer structures that retain silanol groups near the surface (Plueddemann, 1991). In our system, condition (1) is addressed by air plasma treatment, which generates a high density of surface silanols, providing abundant potential bonding sites. For condition (2), we implement a drying step prior to encapsulation and cure the samples at 150 °C. Furthermore, our high levels of surface cleanliness prior to encapsulation, coupled with the saline ageing environment, ionic concentration gradients are likely to drive osmotic water transport away from the interface, helping maintain low interfacial water levels (Donaldson, , 1991; Donaldson and Sayer, 1981). Regarding condition (3), our use of vacuum centrifugation during polymer application (Donaldson and Sayer, 1975), along with the rigid, static nature of the samples, promotes an intimate and stable contact between the polymer and the substrate. Together, these factors may help explain the exceptionally stable adhesion observed in our samples.

5.4.2.4 Thermochemical considerations

Preferential failure (delamination) at alumina substrates rather than at the IC may arise from thermochemical stability differences. Bond dissociation energies of Si–O (799 kJ/mol) significantly exceed Al–O (511 kJ/mol) (Lide, 2004), implying greater resistance of silicon-based interfaces to hydrolysis and thermal stresses, perhaps explaining why delamination over the IC is observed in only one sample. As these are strongly exothermic bonds, elevated temperatures further bias equilibrium toward bond breakage (Le Chatelier's principle) as evidenced by this occurring only in 87 °C samples, and not at lower temperatures.

5.4.2.5 Accelerated ageing vs. physiological conditions

The described failure mode (i.e., blistering), occurring exclusively under combined high temperature (87 °C) and DC bias, exemplifies the potential pitfalls of excessively aggressive accelerated ageing protocols. At physiological temperature (37 °C), such failures are unlikely due to slower kinetics of hydrolysis and diffusion-mediated pH stabilization in biological environments. These findings underscore careful selection of accelerated ageing conditions to avoid artificially induced failure modes absent at physiological conditions (see Supplementary Material 1 for an explanation of the pitfalls of accelerated ageing).

5.4.3 Visible corrosion on solder and pads

The severity of corrosion was strongly associated with temperature, with higher ageing temperatures producing more extensive degradation across both aluminium bond pads and Pb/Sn solder joints (Table 5). The most pronounced corrosion was observed in Batch J (87 °C), where bond pad corrosion ranged from 79% to 83% and solder joint corrosion from 38% to 75%. In contrast, moderate corrosion was seen in Batches G and H (67 °C), while the lowest levels occurred in Batch I (47 °C), demonstrating thermal acceleration of a material degradation process.

The extent of corrosion also varied by pad type. Counter electrode (CE) pads occasionally showed higher corrosion than shield (SH) or working electrode (WE) pads under certain ageing conditions. SH pads tended to exhibit lower solder joint degradation, suggesting that electrode position or function may influence localized corrosion behaviour. However, when comparing total corroded pads across all batches, no single bond pad type (CE, WE, or SH) was consistently more affected. This indicates that corrosion was likely driven by local galvanic interactions and material interfaces rather than the potential differences between the pads. Across all but the highest temperature condition, bond pad corrosion exceeded that of solder joints, but this difference diminished at 87 °C, where both interfaces were severely affected. Solder joint corrosion was more variable overall, likely reflecting localised influences such as flux residues, alloy composition, or intermetallic growth in addition to thermal and electrical stresses.

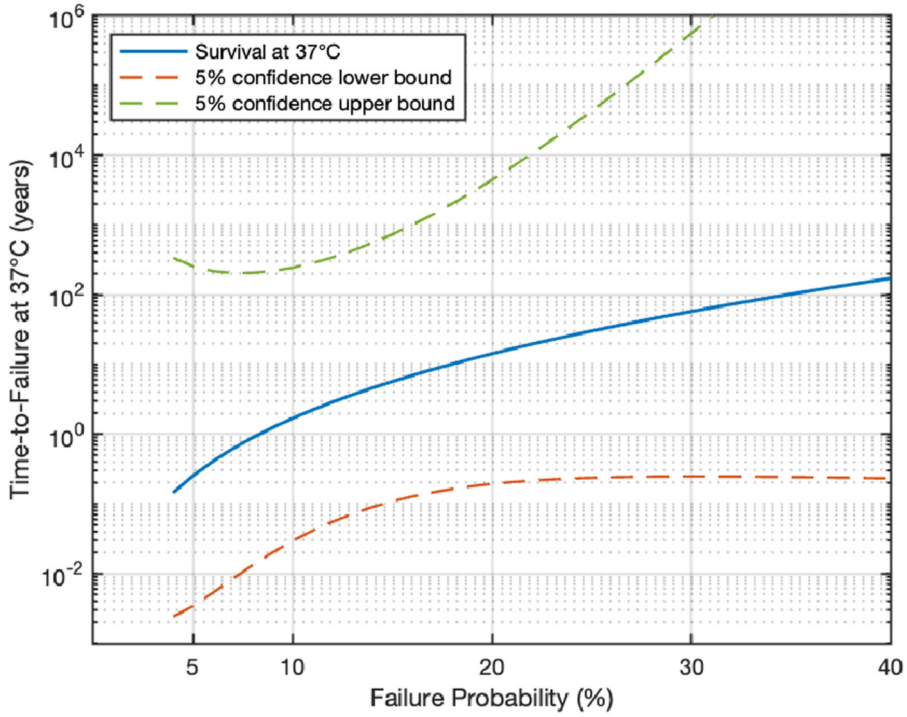

FIGURE 10
Cumulative probability of wire bond failure at 37 ˚C, interpolated from Weibull analysis of failures at 67 ˚C and 87 ˚C. The large confidence interval can be explained by the low β at 67 ˚C.

Interestingly, not all samples exhibiting visual corrosion at the bond pads showed corresponding changes in EIS data. In fact, 40% of samples in Batches G, H, and I presented visible corrosion without any detectable EIS changes. Conversely, no instances of EIS changes were observed without accompanying visual corrosion. This suggests that solder and/or pad corrosion may precede detectable changes in the EIS spectra. However, since visual inspections were conducted at a single time point, we cannot determine whether EIS variations correlate with corrosion onset over time, nor can we establish whether corrosion initiates preferentially at specific bond pads.

5.5 Survival analysis

Although no IC insulation failures were observed in any of the batches, several samples were removed from the ageing experiment owing to interconnection failures and equipment faults (Table 3). Using this data, a survival analysis was performed on the results of Batches H (67 ˚C) and J (87 ˚C). Batch G (67 ˚C, biphasic) and Batch I (47 ˚C) were excluded as there were no relevant failures. The shape parameter β in both batches is less than 1, indicating that the failure rate decreases with time. This is not surprising given the limited number of failures in each batch, and is unlikely to be true in practice, which calls for care in interpreting the scale parameters (η = 51.5 years in Batch H and η = 12.5 years in Batch J). Often called the characteristic life, η indicates the time at which there is a probability that 62.3% of the samples have failed. In fields where the failure of a device can have catastrophic consequences or where replacement is not an option, it may be more interesting to evaluate the time to reach lower cumulative failure probabilities, as done in Figure 10. These results were obtained under accelerated ageing conditions (H at 67 ˚C, J at 87 ˚C, both with 5V DC bias). To infer a lifetime under operating conditions, the acceleration factor between the accelerated and operating conditions must be known. It can be derived from survival data under three accelerated conditions (three data points are the minimum to verify the proportional relation between these conditions). Whilst we did implement three different temperatures with the same bias in Batches H to J, there were no failures in Batch I; hence, we only have two data points. Although our limited data does not enable us to verify it, we make the assumption that the failure reaction rate follows an Arrhenius reaction, and thus the survival time is proportional to $e^{(\frac{1}{T})}$. This assumption was used to extrapolate the cumulative wire bond failure probabilities to 37 ˚C in Figure 10.

5.6 The impact of accelerating conditions

Whilst there were no passivation failures, we can draw a few conclusions on the impact of the experimental conditions and likely causes of failure of future silicone-encapsulated IC implants.

Our work suggests that failure of implants designed with ICs passivated with a SiO_x/SiN_y bilayer and encapsulated with silicone rubber is most likely to be caused by interconnection failure than corrosion of the active area.

Referring to Table 4, temperature does accelerate deterioration. At 47 ˚C, 67 ˚C and 87 ˚C respectively, 50%, 100% and 100% of the

samples observed had visible signs of deterioration, but EIS had changed in only 0%, 29% and 38% of the samples.

In the two batches with failures during ageing, H (67 °C) and J (87 °C), a continuous 5 V bias was applied between the two interdigitated combs. Comparatively, there were no failures in Batch G (67 °C, biphasic bias). Likewise, at the same temperature, there were more changes in the continuous bias (Batch H) than in the biphasic bias (Batch G), 29% versus 0% respectively in EIS changes, and similarly for visual observations, the increase is to 100% from 56%. This may be due to the alternating nature of the biphasic bias, or to the 50% duty cycle. We cannot conclude whether it is the duty cycle or the reversal of potential (that may lead to some reversal of the reactions taking place at the interconnections) that contributes to the lower number of changes in Batch G compared to Batch H.

5.7 Study limitations

The bathing solution used in this experiment was phosphate-buffered saline which matches the pH and osmolality of body fluid but does not imitate all the components of body fluid, and in particular, does not include hydrophobic constituents.

It is known that silicones are impermeable to salts and oxides, while being permeable to non-polar molecules including solvents (e.g., n-heptane, toluene) (Donaldson et al., 2012). The impermeability to salts means that the encapsulant behaves as a semi-permeable membrane (Donaldson, , 1991). However, it is also known that silicones can absorb lipids from the body. Carmen and Kahn found that silicone rubber balls exposed to blood in heart valves gained weight at 0.27% per month, reaching increases as high as 41% and sometimes causing them to & (Carmen and Kahn, 1968). Alterations in mechanical properties have also been reported (Swanson and Lebeau, 1974; Vondráček and Doležel, 1984). There are many hydrophobic compounds in the body that will be preferentially absorbed into silicones rather than water (Yates et al., 2007).

For implants in soft tissue, the bathing liquid would be interstitial fluid. Fatty acids are transported from the capillary membranes to the cells bound to the protein albumin (van der Vusse, 2009). The concentration of these fatty acids depends on recent products of digestion. Despite this binding to albumin, the fatty acids are efficiently transferred to cells.

Several questions arise about silicone implants in soft tissue. How much fatty acid will be absorbed by the encapsulant, how will it be distributed, and how quickly will this happen? What will the effect of the absorption be on the bulk properties (modulus, strength, hardness) and on the adhesion to the underlying surfaces (passivation layer, pads, etc.)?

These questions need to be answered before one could be confident about the longevity of encapsulated implants, though no obvious deleterious effects from hydrophobic constituents have been reported in existing implants with silicone rubber encapsulation as far as we know (Brindley, 1995).

Another species that might affect lifetime is reactive oxygen, produced by the foreign body reaction. Caldwell et al. (2020) have shown that the Parylene-C insulation on Utah Arrays is attacked by reactive oxygen. Although polysiloxanes seem less likely to be affected by a strong oxidising agent, there remains a possibility that it, or other species present in the tissue will have some harmful effect on the device.

Life-testing, possibly accelerated, is a most convincing way to show that a device will survive long enough in operation, but if it takes around 5 years to do so, the chip technology is likely to have changed by the time the evidence has been collected. This may mean that implanted devices must be made from IC technology that is not up-to-date. However, the situation may be less difficult if the properties of the passivation, metallisation, encapsulant are known, and certain design features, such as the seal ring and maximum field-strengths, are maintained.

5.8 Designing implants based on these results

Our IDC chips had two features intended to prevent failure when tested in implant conditions: an additional wall-of-vias and a shield. The area needed for the wall-of-vias is small (Figure 1C), may be required by the foundry, and, as none of these IDC chips showed failure by edge-penetration of water, may have been effective. Walls-of-vias should be used in future implant designs.

The advantage conferred by the shield is less obvious because we saw no dissolution of the passivation layer under the silicone and the shield was intended to prolong lifetime if dissolution occurred. Designers must decide whether or not they can implement the circuit without the top metal layer, so it can be used as extra protection.

As we only had failures related to interconnection, one might assume a silicone-encapsulated fully wireless system with power and communication antenna a trace under passivation, such as in Figure 6 of (Ahmadi et al., 2019), would be an implant architecture that would last long beyond the predictions of this paper.

6 Conclusion

This study set out to evaluate the reliability of silicone-encapsulated CMOS ICs under simulated implant conditions, with the expectation that insulation failures due to water ingress would rapidly occur, due to silicone rubber's high water permeability. Surprisingly, no insulation failures were detected over 4.3 years of accelerated ageing at 47 °C, 67 °C, and 87 °C under electrical bias. Electrochemical impedance spectroscopy (EIS) revealed no significant dielectric insulation degradation, and the foundry passivation layers, encapsulated in adhesive silicone rubber, remained intact under prolonged immersion in hot phosphate-buffered saline.

Instead, the primary failure modes were related to interconnection; gold wire bonds on aluminium pads emerged as the most vulnerable component, exhibiting both infant failures and gradual degradation observed as open circuits. Corrosion of some of these aluminium bond pads was observed, and also corrosion of Pb/Sn solder pads; neither were correlated with EIS changes.

The first aim for future research should be the comparison of better methods for interconnection that avoid the failure modes that are inherent in the gold-on-aluminium welded ball-bond, as discussed in 5.3.2. A further question remains, on the effects of hydrophobic constituents of interstitial fluid.

While we are cautious not to extrapolate a specific lifetime at 37 °C from these data, the absence of insulation failures after 4.3 years of continuous accelerated ageing under electrical bias and elevated temperatures strongly suggests that silicone-encapsulated ICs, thoroughly cleaned and plasma treated pre-encapsulation, can offer robust long-term performance. These findings provide compelling evidence that, when combined with stable foundry passivation, silicone encapsulation is a credible alternative to traditional hermetic enclosures for many miniaturised implantable applications.

Data availability statement

The original contributions presented in the study are included in the article/Supplementary Material, further inquiries can be directed to the corresponding author.

Author contributions

AS: Writing – review and editing, Writing – original draft, Investigation, Software, Validation, Formal Analysis, Data curation, Methodology, Visualization, Conceptualization. CL: Investigation, Conceptualization, Software, Writing – review and editing, Formal Analysis, Writing – original draft, Data curation, Methodology, Visualization. KN: Writing – review and editing. FM: Conceptualization, Validation, Writing – review and editing, Methodology. VG: Resources, Validation, Writing – review and editing, Supervision, Conceptualization, Funding acquisition, Investigation. TC: Investigation, Writing – review and editing, Resources, Funding acquisition, Validation, Conceptualization, Supervision. AV: Project administration, Supervision, Formal Analysis, Validation, Writing – review and editing, Methodology, Conceptualization, Resources, Investigation, Writing – original draft, Funding acquisition, Visualization. ND: Conceptualization, Writing – review and editing, Funding acquisition, Visualization, Software, Investigation, Writing – original draft, Resources, Formal Analysis, Validation, Project administration, Data curation, Supervision, Methodology.

Funding

The author(s) declared that financial support was received for this work and/or its publication. This work was funded by the Wellcome Trust (grant ref: 102037) and the EPSRC (grant ref: NS/A000026/1) as part of the CANDO Innovative Engineering for Health project. It also received support from: Project POSITION-II, funded by the Electronic Components and Systems for European Leadership Joint Undertaking (ECSEL JU) in collaboration with the European Union's H2020 Framework Program (H2020/2014-2020) and National Authorities (grant agreement Ecsel-783132-Position-II-2017-IA); from Toshiba Research UK who supported CL's doctoral work (Studentship Number 000026177); from the Wellcome Trust (WT 218286/Z/19/Z); and also from the General Sir John Monash Foundation who funded ASI's doctoral studentship.

Conflict of interest

AS and TC were employed by Mint Neurotechnologies Ltd., TC is also a director and shareholder.

The remaining author(s) declared that this work was conducted in the absence of any commercial or financial relationships that could be construed as a potential conflict of interest.

Generative AI statement

The author(s) declared that generative AI was not used in the creation of this manuscript.

Any alternative text (alt text) provided alongside figures in this article has been generated by Frontiers with the support of artificial intelligence and reasonable efforts have been made to ensure accuracy, including review by the authors wherever possible. If you identify any issues, please contact us.

Publisher's note

Supplementary material

The Supplementary Material for this article can be found online at: https://www.frontiersin.org/articles/10.3389/felec.2026.1788559/full#supplementary-material

References

Abrecht, C. R., Greenberg, P., Song, E., Urman, R. D., and Rathmell, J. P. (2017). A contemporary medicolegal analysis of implanted devices for chronic pain management. *Anesth. & Analgesia* 124 (4), 1304–1310. doi:10.1213/ANE.0000000000001702

Aceros, J., Yin, M., Borton, D. A., Patterson, W. R., Bull, C., and Nurmikko, A. V. (2012). "Polymeric packaging for fully implantable wireless neural microsensors," in *Proceedings of the Annual International Conference of the IEEE Engineering in Medicine and Biology Society* (New York: Institute of Electrical and Electronics Engineers (IEEE)), 743–746.

Agarwal, A., Shapero, A., Rodger, D., Humayun, M., Tai, Y. C., and Emami, A. (2018). "A wireless, low-drift, implantable intraocular pressure sensor with parylene-on-oil encapsulation," in *2018 IEEE Custom Integrated Circuits Conference (CICC)*.

Ahmadi, N., Cavuto, M., Feng, L., Leene, P., Maslik, M., Mazza, F., et al. (2019). "Towards a distributed, chronically-implantable neural interface," in *2019 9th International IEEE/EMBS Conference on Neural Engineering (NER)*, 719–724.

Ahn, S. H., Jeong, J., and Kim, S. J. (2019). Emerging encapsulation technologies for long-term reliability of microfabricated implantable devices. *Micromachines* 10 (8), 508. doi:10.3390/mi10080508

Andersen, M. A., and Schouenborg, J. (2023). Polydimethylsiloxane as a more biocompatible alternative to glass in optogenetics. *Sci. Rep.* 13 (1), 16090. doi:10.1038/s41598-023-43297-2

Arshad, M. K. M., Hashim, U., and Isa, M. (2007). Under bump metallurgy (UBM): a technology review for flip chip packaging. *Int. J. Mech. Mater. Eng. (IJMME)* 2 (1), 48–54.

Ben-Menachem, E., Revesz, D., Simon, B. J., and Silberstein, S. (2015). Surgically implanted and non-invasive vagus nerve stimulation: a review of efficacy, safety and tolerability. *Eur. J. Neurology* 22 (9), 1260–1268. doi:10.1111/ene.12629

Bachoux, A., Desroches, C., Attik, N., Chiriac, R., Toche, F., and Toury, B. (2024). Minimizing surface adhesion of Sylgard-184 for medical applications. *Appl. Surf. Sci. Adv.* 23, 100624. doi:10.1016/j.apsadv.2024.100624

Bae, W. J., Kim, K. S., Kim, S. J., Cho, H. J., Hong, S. H., Lee, J. Y., et al. (2014). Comparison of biocompatibility between pdms and pmma as packaging materials for the intravesical implantable device: changes of macrophage and macrophage migratory inhibitory factor. *Transl. Androl. Urology* 3 (Suppl. 1), AB222.

Barry, M. P., Sadeghi, R., Towle, V. L., Stipp, K., Grant, P., Lane, F. J., et al. (2023a). Contributed session iii: characteristics of electrically-induced visual percepts in the first human with the intracortical visual prosthesis. *J. Vis.* 23 (11), 35. doi:10.1167/jov.23.11.35

Barry, M. P., Sadeghi, R., Towle, V. L., Stipp, K., Puhov, H., Diaz, W., et al. (2023b). Preliminary visual function for the first human with the intracortical visual prosthesis (ICVP). *Investigative Ophthalmol. Vis. Sci.* 64 (8), 2842.

Barry, M. P., Stipp, K., Towle, V. L., Grant, P., Collison, F. T., Lane, F. J., et al. (2024). Direction-of-motion performance with the intracortical visual prosthesis (ICVP) correlates with visual field coverage. *Investigative Ophthalmol. Vis. Sci.* 65 (7), 4324.

Bernardi, L., Hopf, R., Sibilio, D., Ferrari, A., Ehret, A. E., and Mazza, E. (2017). On the cyclic deformation behavior, fracture properties and cytotoxicity of silicone-based elastomers for biomedical applications. *Polym. Test.* 60, 117–123. doi:10.1016/j.polymertesting.2017.03.018

Bian, P., Wang, Y., and McCarthy, T. J. (2020). Rediscovering silicones: the anomalous water permeability of "hydrophobic" PDMS suggests nanostructure and applications in water purification and anti-icing. *Macromol. Rapid Commun.* 42 (7), 2000682. doi:10.1002/marc.202000682

Bouteiller, L., and Lebarny, P. (1996). Polymer-dispersed liquid crystals: preparation, operation and application. *Liq. Cryst.* 21 (2), 157–174. doi:10.1080/02678299608032820

Brindley, G. S. (1995). The first 500 patients with sacral anterior root stimulator implants: general description. *Spinal Cord.* 33 (12), 795–805. doi:10.1038/sc.1994.126

Brindley, G. S., Polkey, C. E., Rushton, D. N., and Cardozo, L. (1986). Sacral anterior root stimulators for bladder control in paraplegia: the first 50 cases. *J. Neurology, Neurosurg. & Psychiatry* 49 (10), 1104–1114. doi:10.1136/jnnp.49.10.1104

Broccard, F. D., Mullen, T., Chi, Y. M., Peterson, D., Iversen, J. R., Arnold, M., et al. (2014). Closed-loop brain–machine–body interfaces for noninvasive rehabilitation of movement disorders. *Ann. Biomed. Eng.* 42 (8), 1573–1593. doi:10.1007/s10439-014-1032-6

Caldwell, R., Street, M. G., Sharma, R., Takmakov, P., Baker, B., and Rieth, L. (2020). Characterization of Parylene-C degradation mechanisms: *in vitro* reactive accelerated aging model compared to multiyear *in vivo* implantation. *Biomaterials* 232, 119731. doi:10.1016/j.biomaterials.2019.119731

Carmen, R., and Kahn, P. (1968). *In vitro* testing of silicone rubber heart-valve poppets for lipid absorption. *J. Biomed. Mater. Res.* 2 (4), 457–464. doi:10.1002/jbm.820020406

Chang, J. H. C., Liu, Y., Kang, D., and Tai, Y. C. (2013). "Reliable packaging for parylene-based flexible retinal implant," in *2013 Transducers & Eurosensors XXVII: The 17th International Conference on Solid-State Sensors, Actuators and Microsystems* (New York: Institute of Electrical and Electronics Engineers (IEEE)), 2612–2615.

Chen, M. J., Pham, A. V., Evers, N. A., Kapusta, C., Iannotti, J., Kornrumpf, W., et al. (2006). Design and development of a package using lcp for rf/microwave mems switches. *IEEE Trans. Microw. Theory Tech.* 54 (11), 4009–4015. doi:10.1109/tmtt.2006.884639

Chong, H., Majerus, S. J. A., Bogie, K. M., and Zorman, C. A. (2020). Non-hermetic packaging of biomedical microsystems from a materials perspective: a review. *Med. Devices & Sensors* 3 (6), e10082. doi:10.1002/mds3.10082

Chuang, A. T., Margo, C. E., and Greenberg, P. B. (2014). Retinal implants: a systematic review. *Br. J. Ophthalmol.* 98 (7), 852–856. doi:10.1136/bjophthalmol-2013-303708

Coffey, R. J. (2009). Deep brain stimulation devices: a brief technical history and review. *Artif. Organs* 33 (3), 208–220. doi:10.1111/j.1525-1594.2008.00620.x

Colas, A., and Curtis, J. (2004). Silicone biomaterials: history and chemistry. *Biomaterials Sci.*

del Carmen Fuentes, M., Pérez, N., and Ayerdi, I. (2017). Metallization and electrical characterization of platinum thin film microelectrodes on biocompatible polydimethylsiloxane substrates for neural implants. *Thin Solid Films* 636, 438–445. doi:10.1016/j.tsf.2017.06.017

Donaldson, P. E. K. (1973). Experimental visual prosthesis. *Proc. IEE.* 120 (2). doi:10.1049/piee.1973.0061

Donaldson, P. E. K. (1976). The encapsulation of microelectronic devices for long-term surgical implantation. *IEEE Trans. on Biomed. Eng. BME-* 23 (4), 281–285. doi:10.1109/tbme.1976.324586

Donaldson, P. E. K. (1991). Aspects of silicone rubber as an encapsulant for neurological prostheses: part 1 osmosis. *Med. Biol. Eng. Comput.* 29, 34–39. doi:10.1007/BF02446293

Donaldson, P. E. K. (1994). Hydrothermal stability of joints, using a silicone rubber adhesive, for a range of adherends of interest to makers of surgically-implanted microelectronic devices. *Int. Journal Adhesion Adhesives* 14 (2), 103–107. doi:10.1016/0143-7496(94)90004-3

Donaldson, P. E. K. (1995). Aspects of silicone rubber as encapsulant for neurological prostheses: part 3: adhesion to mixed oxides. *Med. Biol. Eng. Comput.* 33, 725–727. doi:10.1007/BF02510794

Donaldson, P. E. K. (1996). The essential role played by adhesion in the technology of neurological prostheses. *Int. Journal Adhesion Adhesives* 16 (2), 105–107. doi:10.1016/0143-7496(95)00031-3

Donaldson, P. E. K., and Aylett, B. J. (1995). Aspects of silicone rubber as encapsulant for neurological prostheses: part 2: adhesion to binary oxides. *Med. Biol. Eng. Comput.* 33, 285–292. doi:10.1007/BF02510501

Donaldson, P. E. K., and Sayer, E. (1975). A vacuum centrifuge for void-free potting of implantable hybrid microcircuits in silicone. *Med. Biol. Eng.* 13, 595–596. doi:10.1007/BF02477144

Donaldson, P. E. K., and Sayer, E. (1977). Silicone-rubber adhesives as encapsulants for microelectronic implants; effect of high electric fields and of tensile stress. *Med. Biol. Eng. Comput.* 15, 712–715. doi:10.1007/BF02457937

Donaldson, P. E. K., and Sayer, E. (1981). Osmotic pumping of non-hermetic neuroprosthetic implants. *Med. Biol. Eng. Comput.* 19 (4), 483–485. doi:10.1007/BF02441316

Donaldson, N., Baviskar, P., Cunningham, J., and Wilson, D. (2012). The permeability of silicone rubber to metal compounds: relevance to implanted devices. *J. Biomed. Mater. Res. Part A* 100 (3), 588–598. doi:10.1002/jbm.a.33257

Donaldson, N., Lamont, C., Shah Idil, A., Mentink, M., and Perkins, T. (2018). Apparatus to investigate the insulation impedance and accelerated life-testing of neural interfaces. *J. Neural Eng.* 15 (6), 066034. doi:10.1088/1741-2552/aadeac

Firfilionis, D., Hutchings, F., Tamadoni, R., Walsh, D., Turnbull, M., Escobedo-Cousin, E., et al. (2021). A closed-loop optogenetic platform. *Front. Neurosci.* 15, 718311. doi:10.3389/fnins.2021.718311

Frederick, R. A., Shih, E., Towle, V. L., Joshi-Imre, A., Troyk, P. R., and Cogan, S. F. (2022). Chronic stability of activated iridium oxide film voltage transients from wireless floating microelectrode arrays. *Front. Neurosci.* 16, 876032. doi:10.3389/fnins.2022.876032

Gent, A. N., and Lindley, P. B. (1959). Internal rupture of bonded rubber cylinders in tension. *Proc. R. Soc. Lond. Ser. A. Math. Phys. Sci.* 249 (1257), 195–205. doi:10.1098/rspa.1959.0016

Grant, P., Barry, M. P., Stipp, K., Jiang, A., Towle, V. L., Sadeghi, R., et al. (2024). Camera testing of an intracortical visual prosthesis for identifying occupied and vacant chairs. *Investigative Ophthalmol. Vis. Sci.* 65 (7), 4325.

Greatbatch, W. (2000). *The making of the pacemaker: celebrating a lifesaving invention.* Amherst, New York: Prometheus Books.

Griffin, A. J., Hernandez, S. E., Brotzen, F. R., and Dunn, C. F. (1994). A galvanic series for thin-film metallizations and barrier layers commonly used in the microelectronics industry. *J. Electrochem. Soc.* 141 (3), 807–809. doi:10.1149/1.2054815

Guljakow, J., and Lang, W. (2023). Analysis of the lifetime of neural implants using *in vitro* test structures. *Sensors* 23 (14), 6263. doi:10.3390/s23146263

Ha, D., Kim, B. G., Lin, T. Y., Ouyang, Y., Irazoqui, P., and Chappell, W. J. (2010). "3d packaging technique on liquid crystal polymer (lcp) for miniature wireless biomedical sensor," in *IEEE MTT-S International Microwave Symposium Digest*, 612–615.

HajjHassan, M., Chodavarapu, V., and Neuromems, S. M. (2008). Neural probe microtechnologies. *Sensors* 8 (10), 6704–6726.

Harman, G. G. (2010). *Wire bonding in microelectronics.* 3rd edition. McGraw-Hill.

Jeng, S.-P., Hsu, S.-H., Hou, S.-Y., Tsai, H.-Y., and Yu, C.-H. (2008). Seal ring structure with improved cracking protection. *U. S. Pat. Appl. US20080283969A1.*

Jeong, J., Lee, S. W., Min, K. S., Shin, S., Jun, S. B., and Kim, S. J. (2012). Liquid crystal polymer (lcp), an attractive substrate for retinal implant. *Sensors Mater.* 24 (4), 189–203.

Jeong, J., Shin, S., Lee, G. J., Gwon, T. M., Park, J. H., and Kim, S. J. (2013). "Advancements in fabrication process of microelectrode array for a retinal prosthesis using liquid crystal polymer (lcp)," in *Proceedings of the Annual International Conference of the IEEE Engineering in Medicine and Biology Society* (New York: Institute of Electrical and Electronics Engineers (IEEE)), 5295–5298.

Jeong, J. W., McCall, J. G., Shin, G., Zhang, Y., Al-Hasani, R., Kim, M., et al. (2015). Wireless optofluidic systems for programmable *in vivo* pharmacology and optogenetics. *Cell* 162, 662–674. doi:10.1016/j.cell.2015.06.058

Jeong, J., Bae, S. H., Min, K. S., Seo, J. M., Chung, H., and Kim, S. J. (2015). A miniaturized, eye-conformable, and long-term reliable retinal prosthesis using monolithic fabrication of liquid crystal polymer (lcp). *IEEE Trans. Biomed. Eng.* 62 (3), 982–989. doi:10.1109/TBME.2014.2377197

Jiang, A., Dagnelie, G., Grant, P., Barry, M. P., Szlyk, J. P., Sorci, G., et al. (2024). Visual prosthesis aids walking direction discrimination in a blind individual. *Investigative Ophthalmol. Vis. Sci.* 65 (7), 2586.

Kassiri, H., Tonekaboni, S., Salam, M. T., Soltani, N., Abdelhalim, K., Velazquez, J. L. P., et al. (2017). Closed-loop neurostimulators: a survey and a seizure-predicting design example for intractable epilepsy treatment. *IEEE Trans. Biomed. Circuits Syst.* 11 (5), 1026–1040. doi:10.1109/TBCAS.2017.2694638

Kim, D. H., Lu, N., Ma, R., Kim, Y. S., Kim, R. H., Wang, S., et al. (2011). Epidermal electronics. *Science* 333, 838–843. doi:10.1126/science.1206157

Kinloch, A. J. (2012). *Adhesion and adhesives: science and technology*. Dordrecht: Springer Science & Business Media.

Klinge, P. M., Vafa, M. A., Brinker, T., Brandis, A., Walter, G. F., Stieglitz, T., et al. (2001). Immunohistochemical characterization of axonal sprouting and reactive tissue changes after long-term implantation of a polyimide sieve electrode to the transected adult rat sciatic nerve. *Biomaterials* 22 (17), 2333–2343. doi:10.1016/s0142-9612(00)00420-8

Kuliasha, C. A., and Judy, J. W. (2018). "*In vitro* reactive-accelerated-aging (raa) assessment of tissue-engineered electronic nerve interfaces (teeni)," in *Proceedings of the 2018 40th Annual International Conference of the IEEE Engineering in Medicine and Biology Society (EMBC)* (IEEE), 5061–5064.

Kuliasha, C. A., and Judy, J. W. (2019). "*In vitro* reactive-accelerated-aging assessment of anisotropic conductive adhesive and back-end packaging for electronic neural interfaces," in *Proceedings of the 2019 41st Annual International Conference of the IEEE Engineering in Medicine and Biology Society (EMBC)* (IEEE), 3766–3769.

Kuo, H. I., Zhang, R., and Ko, W. H. (2010). Development of micropackage technology for biomedical implantable microdevices using Parylene-C as water vapor barrier coatings. *Proc. SENSORS, 2010 IEEE*, Waikoloa, HI, 438–441. doi:10.1109/ICSENS.2010.5690184

Lacour, S. P., Benmerah, S., Tarte, E., FitzGerald, J., Serra, J., McMahon, S., et al. (2010). Flexible and stretchable micro-electrodes for *in vitro* and *in vivo* neural interfaces. *Med. & Biol. Eng. & Comput.* 48, 945–954. doi:10.1007/s11517-010-0644-8

Lamont, C. (2020). *Non-Hermetic protection of implanted thin film and CMOS electronic medical devices*. London, UK: University College London. Phd thesis.

Lamont, C., Grego, T., Nanbakhsh, K., Shah Idil, A., Giagka, V., Vanhoestenberghe, A., et al. (2021). Silicone encapsulation of thin-film SiOx, SiOx Ny and SiC for modern electronic medical implants: a comparative long-term ageing study. *J. Neural Eng.* 18 (5), 055003. doi:10.1088/1741-2552/abf0d6

Lecomte, A., Degache, A., Descamps, E., Dahan, L., and Bergaud, C. (2017). *In vitro* and *in vivo* biostability assessment of chronically-implanted Parylene-C neural sensors. *Sensors Actuators B Chem.* 251, 1001–1008. doi:10.1016/j.snb.2017.05.057

Lee, S. W., Seo, J. M., Ha, S., Kim, E. T., Chung, H., and Kim, S. J. (2009). Development of microelectrode arrays for artificial retinal implants using liquid crystal polymers. *Investigative Ophthalmol. & Vis. Sci.* 50 (12), 5859–5866. doi:10.1167/iovs.09-3743

Lee, S. W., Min, K. S., Jeong, J., Kim, J., and Kim, S. J. (2011). Monolithic encapsulation of implantable neuroprosthetic devices using liquid crystal polymers. *IEEE Trans. Biomed. Eng.* 58 (8), 2255–2263. doi:10.1109/tbme.2011.2136341

Lide, D. R. (2004). *CRC handbook of chemistry and physics, 85th edition*. Boca Raton, FL: Taylor & Francis.

Liu, D., and Broer, D. J. (2014). Liquid crystal polymer networks: preparation, properties, and applications of films with patterned molecular alignment. *Langmuir* 30 (45), 13499–13509. doi:10.1021/la500454d

Martini, M. L., Oermann, E. K., Opie, N. L., Panov, F., Oxley, T., and Yaeger, K. (2020). Sensor modalities for brain-computer interface technology: a comprehensive literature review. *Neurosurgery* 86 (2), E108–E117. doi:10.1093/neuros/nyz286

Mathews, R. P., Habibagahi, I., Jafari Sharemi, H., Challita, R., Cha, S., and Babakhani, A. (2025). A closed loop fully automated wireless vagus nerve stimulation system. *Sci. Rep.* 15 (1), 27856. doi:10.1038/s41598-025-11159-8

Mc Laughlin, M., Lu, T., Dimitrijevic, A., and Zeng, F. G. (2012). Towards a closed-loop cochlear implant system: application of embedded monitoring of peripheral and central neural activity. *IEEE Trans. Neural Syst. Rehabilitation Eng.* 20 (4), 443–454. doi:10.1109/TNSRE.2012.2186982

Nanbakhsh, K., Shah Idil, A., Lamont, C., Dücső, C., Akgun, Ö. C., Horváth, D., et al. (2025). Lamont. On the longevity and inherent hermeticity of silicon-ICs: evaluation of bare-die and PDMS-coated ICs after accelerated aging and implantation studies. *Nat. Commun.* 16, 12. doi:10.1038/s41467-024-55298-4

Naples, J. G., and Ruckenstein, M. J. (2020). Cochlear implant. *Otolaryngologic Clin. N. Am.* 53 (1), 87–102. doi:10.1016/j.otc.2019.09.004

Noh, H. S., Huang, Y., and Hesketh, P. J. (2004). Parylene micromolding, a rapid and low-cost fabrication method for parylene microchannel. *Sensors Actuators B Chem.* 102 (1), 78–85. doi:10.1016/j.snb.2003.09.038

Ortigoza-Diaz, J., Scholten, K., Larson, C., Cobo, A., Hudson, T., Yoo, J., et al. (2018). Techniques and considerations in the microfabrication of Parylene-C microelectromechanical systems. *Micromachines* 9 (9), 422. doi:10.3390/mi9090422

Osenbach, J. W. (1993). Water-induced corrosion of materials used for semiconductor passivation. *J. Electrochem. Soc.* 140 (12), 3667–3675. doi:10.1149/1.2221147

Parastarfeizabadi, M., and Kouzani, A. Z. (2017). Advances in closed-loop deep brain stimulation devices. *J. Neuroeng. Rehabil.* 14 (1), 79. doi:10.1186/s12984-017-0295-1

Park, J. H., Jeong, J., Moon, H., Kim, C., and Kim, S. J. (2016). Feasibility of lcp as an encapsulating material for photodiode-based retinal implants. *IEEE Photonics Technol. Lett.* 28, 1. doi:10.1109/lpt.2016.2523561

Park, S., Mondal, K., Treadway, R. M., III, Kumar, V., Ma, S., Holbery, J. D., et al. (2018). Silicones for stretchable and durable soft devices: beyond Sylgard-184. *ACS Appl. Mater. & Interfaces* 10 (13), 11261–11268. doi:10.1021/acsami.7b18394

Plueddemann, E. P. (1991). *Nature of adhesion through silane coupling agents*. US, Boston, MA: Springer, 115–152.

Pourmodheji, R., Qu, S., and Yu, H. (2018). Two possible defect growth modes in soft solids. *J. Appl. Mech.* 85 (3), 031001. doi:10.1115/1.4038718

Rezai, P., Selvaganapathy, P. R., and Wohl, G. R. (2011). "Plasma enhanced bonding of polydimethylsiloxane (pdms) with parylene," in *2011 16th International Solid-State Sensors, Actuators and Microsystems Conference (TRANSDUCERS'11)*.

Rodger, D. C., Weiland, J. D., Humayun, M. S., and Tai, Y. C. (2006). Scalable high lead-count parylene package for retinal prostheses. *Sensors Actuators B Chem.* 117 (1), 107–114. doi:10.1016/j.snb.2005.11.010

Rubehn, B., and Stieglitz, T. (2010). *In vitro* evaluation of the long-term stability of polyimide as a material for neural implants. *Biomaterials* 31 (13), 3449–3458. doi:10.1016/j.biomaterials.2010.01.053

Shit, S. C., and Shah, P. (2013). A review on silicone rubber. *Natl. Acad. Sci. Lett.* 36 (4), 355–365. doi:10.1007/s40009-013-0150-2

Saeidi, N., Flynn, M., Byun, K. Y., Yu, R., Ferain, I., Colinge, C., et al. (2010). Developing a wafer level gold-polysilicon eutectic bond process to protect sensitive electronic devices. *ECS Trans.* 33 (4), 83–89. doi:10.1149/1.3483496

Shapero, A., Liu, Y., and Tai, Y. C. (2016). "Parylene-on-oil packaging for implantable pressure sensors," in *Proceedings of the IEEE International Conference on Micro Electro Mechanical Systems (MEMS)*.

Shepherd, R. K. (2016). *Neurobionics: the biomedical engineering of neural prostheses* (United Kingdom: Wiley).

Sim, S. P., and Lawson, R. W. (1979). "The influence of plastic encapsulants and passivation layers on the corrosion of thin Aluminium Films subjected to humidity stress," in 17th International Reliability Physics Symposium, San Diego, CA, 103–112. doi:10.1109/IRPS.1979.362878

Stark, N. (1996). Literature review: biological safety of Parylene-C. *Med. Plastic Biomaterials* 3, 30–35.

Street, M. G., Welle, C. G., and Takmakov, P. A. (2018). Automated reactive accelerated aging for rapid *in vitro* evaluation of neural implant performance. *Rev. Sci. Instrum.* 89 (9), 094301. doi:10.1063/1.5024686

Swanson, J. W., and Lebeau, J. E. (1974). The effect of implantation on the physical properties of silicone rubber. *J. Biomed. Mater. Res.* 8 (6), 357–367. doi:10.1002/jbm.820080603

Takmakov, P., Ruda, K., Phillips, K. S., Isayeva, I. S., Krauthamer, V., and Welle, C. G. (2015). Rapid evaluation of the durability of cortical neural implants using accelerated aging with reactive oxygen species. *J. Neural Eng.* 12 (2), 026003. doi:10.1088/1741-2560/12/2/026003

Tan, C. P., and Craighead, H. G. (2010). Surface engineering and patterning using parylene for biological applications. *Materials* 3 (3), 1803–1832. doi:10.3390/ma3031803

The Dow Chemical Company (2017). *DOWSIL™ 96-083 silicone adhesive: product information sheet*

Troyk, P. (2015). "Preparation for the implantation of an intracortical visual prosthesis in a human: Final report (FY 2015)," in *Technical report AD1016261, U.S. army medical research and materiel command* (Fort Detrick, MD: U.S. Army Medical Research and Materiel Command/Defense Technical Information Center).

Troyk, P. (2013). "Preparation for the implantation of an intracortical visual prosthesis in a human: annual report (FY 2013)," in *Technical Report ADA612547, U.S. Army Medical Research and Materiel Command* (Fort Detrick, MD: U.S. Army Medical Research and Materiel Command / Defense Technical Information Center).

Troyk, P. (2014). "Preparation for the implantation of an intracortical visual prosthesis in a human: annual report (FY 2014)," in *Technical Report ADA622258, U.S. Army Medical Research and Materiel Command* (Fort Detrick, MD: U.S. Army Medical Research and Materiel Command / Defense Technical Information Center).

Troyk, P. (2017). "The intracortical visual prosthesis project," in *Artificial vision: a clinical guide*, 203–214.

van der Vusse, G. (2009). Albumin as fatty acid transporter. *Drug Metabolism Pharmacokinetics* 24 (4), 300–307. doi:10.2133/dmpk.24.300

Vanherck, K., Koeckelberghs, G., and Vankelecom, I. F. J. (2013). Crosslinking polyimides for membrane applications: a review. *Prog. Polym. Sci.* 38 (6), 874–896. doi:10.1016/j.progpolymsci.2012.11.001

Vanhoestenberghe, A., and Donaldson, N. (2011). The limits of hermeticity test methods for micropackages. *Artif. Organs* 35 (3), 242–244. doi:10.1111/j.1525-1594.2011.01222.x

Vanhoestenberghe, A., and Donaldson, N. (2013). Corrosion of silicon integrated circuits and lifetime predictions in implantable electronic devices. *J. Neural Eng.* 10 (3), 031002. doi:10.1088/1741-2560/10/3/031002

Vondráček, P., and Doležel, B. (1984). Biostability of medical elastomers: a review. *Biomaterials* 5 (4), 209–214. doi:10.1016/0142-9612(84)90017-6

White, M. L. (1969). Encapsulation of integrated circuits. *Proc. IEEE* 57 (9), 1610–1615. doi:10.1109/proc.1969.7344

Woods, V., Trumpis, M., Bent, B., Palopoli-Trojani, K., Chiang, C.-H., Wang, C., et al. (2018). Long-term recording reliability of liquid crystal polymer μECOG arrays. *J. Neural Eng.* 15 (6), 066019. doi:10.1088/1741-2552/aae39d

Yates, K., Davies, I., Webster, L., Pollard, P., Lawton, L., and Moffat, C. (2007). Passive sampling: partition coefficients for a silicone rubber reference phase. *J. Environ. Monit.* 9 (10), 1116–1121. doi:10.1039/b706716j

Zaaimi, B., Turnbull, M., Hazra, A., Wang, Y., Gandara, C., McLeod, F., et al. (2022). Hazra. Closed-loop optogenetic control of the dynamics of neural activity in non-human primates. *Nat. Biomed. Eng.* 7 (4), 559–575. doi:10.1038/s41551-022-00945-8